Atmospheric
Measurement
Techniques
Discussions

Instabilities, Dynamics, and Energetics accompanying Atmospheric Layering (IDEAL) Campaign: High-Resolution in situ Observations above the Nocturnal Boundary Layer

Abhiram Doddi[1], Dale Lawrence[1], David Fritts[2], Ling Wang[2], Thomas Lund[2], William Brown[3], Dragan Zajic[4], and Lakshmi Kantha[1]

[1]Smead Aerospace Engineering Sciences, University of Colorado, Boulder, CO, USA
[2]GATS, Boulder, CO, USA
[3]Earth Observing Laboratory, National Center for Atmospheric Research, Boulder, CO, USA
[4]Meteorology Division, Dugway Proving Ground, Dugway, UT, USA

Correspondence: Abhiram Doddi (abhiram.doddi@colorado.edu); Dale Lawrence (dale.lawrence@colorado.edu); David Fritts (dave@gats-inc.com); Ling Wang (lwang@gats-inc.com); Thomas Lund (t.lund@gats-inc.com); William Brown (wbrown@ucar.edu); Dragan Zajic (dragan.zajic.civ@mail.mil); Lakshmi Kantha (kantha@colorado.edu)

Abstract. The Instabilities, Dynamics, and Energetics accompanying Atmospheric Layering (IDEAL) project was conceived to improve our understanding of the dynamics of sheet and layer (S&L) structures in the lower troposphere under strongly stable conditions. The approach employed a synergistic combination of targeted multi-point observations using small unmanned aircraft systems (sUAS) guiding direct numerical simulation (DNS) modeling to characterize the dynamics driving the S&L

5   structures and associated flow features. The IDEAL research program consisted of two phases. The first was an observational field campaign to systematically probe stable lower atmosphere conditions using multiple DataHawk-2 (DH2) sUAS. Coordinated, simultaneous multi-DH2 flights were guided by concurrent Integrated Sounding System (ISS) wind profiler radar and radiosonde soundings performed by NCAR Earth Observing Laboratory (EOL) participants. Additional sUAS flight guidance was obtained from real-time sUAS measurements. Following the field campaign, the second phase focused on high-resolution

10 DNS modeling efforts guided by in-situ observations made during the first phase. This overview focuses on the details of the observational phase that took place from 24 October to 15 November 2017 at Dugway Proving Ground (DPG), Utah. A total of 72 DH2 flights coordinated with 93 balloon-borne radiosondes were deployed in support of the IDEAL field campaign. Our discussion addresses the average atmospheric conditions, the observation strategy, and the objectives of the field campaign. Also presented are representative flight sorties and sUAS environmental and turbulence measurements.

15

1 Introduction

Under stable conditions, the vertical structure of the atmosphere is characterized by thin, strongly stable non-turbulent "sheets" separated by thicker, less stable and often weakly turbulent "layers" (Gage and Green, 1978; Röttger and Liu, 1978). These sheet and layer (S&L hereafter) structures are often observed in temperature, humidity, and horizontal winds within the lower troposphere (Balsley et al., 2006, 2003; Chimonas, 1999; Mahrt, 1999; Xing-Sheng et al., 1983; Kantha et al., 2019) and into the edge of the Stratosphere (Barat, 1982; Fairall et al., 1991; Gage and Balsley, 1980; Röttger, 1980; Woodman and Guillen, 1974). The S&L structures are known to play an important role in the transport and mixing of heat, momentum, and constituents (Barat, 1982; Chimonas, 1999; Dalaudier et al., 1994; Hunt et al., 1985), as well as important roles in optical (Coulman et al., 1995) and radio wave propagation (Gossard et al., 1984; Luce et al., 2001; Röttger, 1980; Xing-Sheng et al., 1983).

The large-scale vertical features of the layering structures have been qualitatively analyzed using monostatic and bistatic VHF radar observations (Balsley et al., 2006, 2003; Dalaudier et al., 1994; Luce et al., 2001, 1995; Woodman and Chu, 1989). Details have been characterized in terms of typical sheet thickness and stability, thickness of turbulent layers, Richardson Number, and turbulence Reynolds number through in-situ measurements from soundings, stationary observation towers and tethered lifting systems (TLS) (Balsley et al., 2003, 2006; Muschinski et al., 2001a), and more recently, using aircraft (Lawrence and Balsley, 2013; Muschinski and Wode, 1998). High-resolution multi-point measurements of temperature (Barat, 1982; Coulman, 1973; Frehlich et al., 2003; Hunt et al., 1985; Xing-Sheng et al., 1983) and VHF radar estimates (and comparison with theoretical models) of refractive index structure function (C_n^2) (VanZandt et al., 1978; Woodman and Guillen, 1974) have established the intermittent nature of turbulence within deep layers. More recently, quantitative aircraft measurements of turbulence kinetic energy dissipation rate (ϵ) and the temperature structure function (C_T^2) have characterized the small-scale turbulence features within shallow layers (Balsley et al., 2018; Eaton et al., 1998; Fernando et al., 2015; Muschinski et al., 2001b; Scipión et al., 2016).

Various explanations for the prevalence of S&L structures have been proposed. Concurrent observations using VHF radars and in-situ measurements suggest that S&L are the result of multi-scale gravity waves (GWs) interacting with the fine structure (FS) of the background atmosphere (Barat, 1982; Coulman et al., 1995; Luce et al., 1995; Röttger, 1980). Various analytical studies and numerical modeling results support this conjecture (Fairall et al., 1991; Fritts and Rastogi, 1985; Fritts et al., 2009a; Fua et al., 1982; Sidi et al., 1988; Smith et al., 1987; VanZandt et al., 1978). More recent Direct Numerical Simulations (DNS) achieving very high spatial and temporal resolution, primarily addressing multi-scale GW-FS interactions in "stable" environments (Fritts and Wang, 2013; Fritts et al., 2009b, 2013), suggest that Kelvin-Helmholtz instabilities (KHI), GW breaking and intrusions lead to the formation of S&L. Tjernström et al. (2009) suggested that air flow over low-relief terrain (i.e., small-scale mountain waves) are a plausible formation mechanism for S&L in the lower troposphere.

However, a deeper understanding of the formation, morphology, and evolution of S&L is hampered by current observational methods that are limited by spatial and temporal resolution, and inadequate range and dexterity of measurement platforms (Chimonas, 1999; Muschinski et al., 2001a; Muschinski and Wode, 1998; Tjernström et al., 2009). Additionally, the single-point vertical profiles (instrumented towers, balloon borne soundings, and TLS) provide little information about the lateral scales

50   of S&L structures (Muschinski and Wode, 1998). The limited lateral-scale characterization and the dearth of high-resolution, quantitative measures of turbulence parameters provide poor guidance for modeling studies employing high-resolution DNS.

The Instabilities, Dynamics, and Energetics accompanying Atmospheric Layering (IDEAL) project was conceived to address this limitation through a synergistic combination of precisely targeted multi-point observations using small unmanned aircraft system (sUAS) guiding DNS modeling to characterize the dynamics driving S&L structures and associated flow features. The

55   first phase of the project featured an observational field campaign to systematically probe stable lower atmosphere conditions using multiple University of Colorado DataHawk-2 (DH2) unmanned aircraft, guided by NCAR Integrated Sounding System (ISS) continuous radar profiling, hourly radiosonde profiling. Measurements were conducted employing multiple-DH2, most-commonly in sorties of three aircraft, for in situ profiling and horizontal and/or slant path sampling. A total of 72 DH2 flights coordinated with 93 balloon-borne radiosondes were deployed in support of the IDEAL field campaign. Additionally, an array

60   of Surface Atmospheric Measurement Systems (SAMS) collected surface winds, temperature, and relative humidity at 2 m (called mini-SAMS) and 10 m (called SAMS) to monitor surface and boundary layer activity. Observation locations of IDEAL field measurements are shown in Figure 1. Following the field campaign, the second phase focused on high-resolution DNS modeling efforts, guided by the in situ observations, to permit more quantitative exploration of S&L formation mechanisms, evolution, and morphology.

65   This article focuses on the details of the observational phase that took place between 24 October and 15 November of 2017 at the Dugway Proving Ground (DPG), Utah. Section 2 outlines the meteorological conditions during the campaign, the observation platforms used, and the data obtained. Section 3 describes typical measurement strategies employed. Section 4 illustrates preliminary findings from DH2 data. Section 5 describes implications of the IDEAL measurement program for IDEAL and related modeling of sheet and layer structures and dynamics. Finally, section 6 provides concluding remarks and
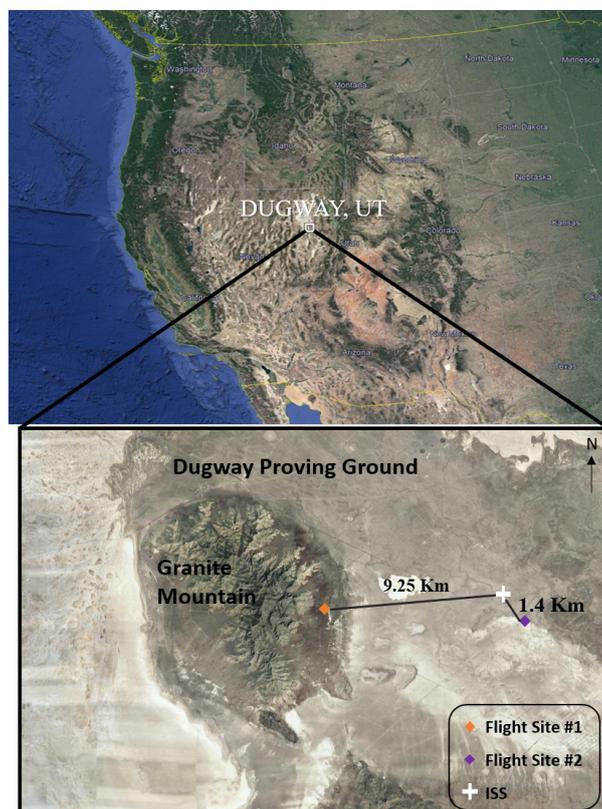
70   the scope for future work.

Figure 1. IDEAL field campaign location at DPG, Utah (top). The satellite image shows locations of UAS observation sites (orange and purple diamonds) and the ISS deployment site (white cross). The satellite imagery obtained from © Google Earth 3D mapping tool.

2 Measurement Platforms and Observed Meteorological Conditions

2.1 DataHawk sUAS

The DH2 sUAS used for IDEAL measurements (see Figure 2, and Table 1 & 2) is a product of many years of development at the University of Colorado. It is specifically designed for making high-resolution in-situ observations in the lower troposphere, and for operations in challenging surface conditions. The precursor DH1 was used in campaigns in Peru (Balsley et al., 2013; Lawrence and Balsley, 2013; Scipión et al., 2016) and Utah (Balsley et al., 2018; Fernando et al., 2015). The DH2 was used in campaigns in Japan (Kantha et al., 2017, 2019; Luce et al., 2018a, b, 2019, 2017), Colorado (de Boer et al., 2019), and Alaska (de Boer et al., 2018). Altogether, over 650 science flights have been performed with the DH2, totaling 430 flight hours. Relevant attributes of DH2 sUAS deployed during the IDEAL field program are noted below:

- **Low cost.** At approximately $1,000 each, many vehicles can be deployed for a campaign, enabling multiple simultaneous measurements (as employed extensively for IDEAL) or sequences of overlapping flights to provide continuous

4

measurements over many hours. This also enables observations in marginal conditions (e.g., high winds) that would ground more expensive vehicles due to the risk of loss. Ten DH2 vehicles were brought to the 23 day IDEAL campaign.

- **Ruggedness.** The airframe is resilient foam, strengthened by a system of interior spars and flexures that absorb impacts, enabling the vehicle to "bounce" rather than break when landing on unprepared surfaces. It has a no-tail design, since these extended members are easily broken, and unbreakable wing trailing edges and vertical fins. It also has a rear propeller with folding blades to prevent damage to the propulsion system during landing. In the IDEAL campaign, five DH2 aircraft were used extensively, of which two were retired due to accumulated wear. No aircraft were lost.

- **Ease of operation.** A custom autopilot provides automatic launch, landing, and vector field flight control (Lawrence et al., 2008), enabling a variety of measurement strategies to be set up with ease and flown under minimal operator supervision. Flight patterns can also be changed during flight to target specific volumes of interest, e.g., based on real-time measurements—an ability that was extensively used during IDEAL to identify and more thoroughly sample turbulence fields. A bungee cord is used for launch, guided by a simple two-rail launch ramp (see Figure 2).

- **Gust-insensitive design.** The unique aerodynamic design eliminates the roll moment due to sideslip, making the vehicle point into gusts rather than roll away from it, enabling well-behaved flight in high-wind and strong turbulence conditions. Normally, flights are not performed when surface winds exceed $10\,\mathrm{ms^{-1}}$, or predicted winds aloft exceed $15\,\mathrm{ms^{-1}}$. The vector field guidance uses a wind-aware algorithm to stabilize flight even when wind speed exceeds airspeed. During IDEAL, synoptic winds aloft often exceeded $20\,\mathrm{ms^{-1}}$, limiting the flight ceiling to about $3\,\mathrm{km}$.

- **Flexible sensor interfacing.** The custom DataHawk autopilot provides multiple serial interfaces (7 UART, 3 I2C, 4 SPI), enabling a variety of sensors to be supported, and their data stored on-board (micro SD card), and telemetered to the ground station for real time display. Tables 1 and 2 provide details of the sensors employed for IDEAL. Sensors can be installed at various locations in the body or the wings of the airframe without altering the flight dynamics.

- **Efficiency.** Flight durations exceed $80\,\mathrm{min}$, making altitudes of $5\,\mathrm{km}$ above a ground launch accessible with a typical $2\,\mathrm{ms^{-1}}$ ascent/descent rate, and a lateral range (out and back) of $30\,\mathrm{km}$ at a nominal airspeed of $15\,\mathrm{ms^{-1}}$.

Figure 2. DH2 sUAS ready for launch at DPG during the IDEAL campaign.

105   For IDEAL, the DH2 was configured to make the following in-situ observations.

1. **Measurement location and time.** A UBlox M8N single-frequency GPS receiver provides horizontal position data and time at 5 Hz cadence. Altitude measurement is refined in post-flight analysis, to obtain high-vertical resolution, by calibrating the higher rate of response (100 Hz) barometric pressure altitude against the low-rate (~ 5 Hz) GPS altitude. Similarly, sensor measurement times are recorded at high-resolution by calibrating 10 microsecond microprocessor timer

110   ticks to GPS time of week (TOW) data in post-flight time-alignment procedures.

2. **Mean atmospheric state.** Temperature and relative humidity (T/RH) are provided by a Sensirion SHT-31, located in the flow stream inside a cylindrical shroud, mounted above the vehicle as shown in Figure 2. Pressure is provided by a TE MS5611 absolute pressure sensor, located in an unsealed compartment within the foam aircraft body.

3. **High-resolution temperature.** A custom (coldwire) thermometer uses a five micrometer diameter platinum wire to

115   detect fine-scale temperature variations in the flow. With a time constant of 0.5 millisecond and a sampling rate of 800 Hz, temperature variations at wavenumbers of ~ 25 m^{-1} can be detected at the nominal 15 ms^{-1} airspeed. The temperature is calibrated against the collocated (but slow) SHT temperature (to kelvin) in post flight analysis and used with high-resolution altitude to obtain high-vertical resolution potential temperature θ. Spectral analysis is also used to fit inertial sub-range power spectral density models to provide estimates of the turbulent temperature structure parameter

120   C_T^2.

4. **High-resolution airspeed.** A custom pitot-static tube and a TE MS4515 differential pressure sensor provide 800 Hz airspeed data that is calibrated to ms^{-1}. Wavenumber resolutions simlilar to temperature fluctuations are obtained in velocity variations also, and spectral estimation methods are used to derive turbulent kinetic energy dissipation rate ϵ. Filtered airspeed data are also used to estimate winds (described below). In addition, a custom (hotwire) anemometer uses a second 5 micrometer diameter platinum wire to detect fine-scale velocity variations, and these are also used to estimate ϵ, but at higher confidence level due to the absence of motor vibration artifacts that typically appear in the pitot velocity spectra at high frequencies.

5. **Horizontal Wind.** Vehicle GPS velocity is combined with pitot airspeed and vehicle attitude to produce estimates of the horizontal wind at 1 Hz cadence in post flight analysis.

6. **Atmospheric stability.** The Brunt-Vaisala (buoyancy) frequency is evaluated using vertical gradient of high-resolution potential temperature θ.

7. **Forcing conditions.** Destabilizing horizontal wind shear is assessed relative to the background layer stability via the gradient Richardson number, derived from the horizontal mean wind gradient with altitude, and the local buoyancy frequency.

DH2 Characteristics		DH2 Capabilities	
Wingspan	1.3 m	Airspeed	10-20 ms^{-1}
Mass	1.3 kg	Duration	80 minutes
Vehicle Cost	$1000	Range (one way)	60 km
Sensor Cost	$400	Altitude (balloon Drop)	6 km AGL
Design	Flying wing, rear propeller	Altitude (ground launch)	5 km AGL
Telemetry	IEEE 802.15.4, 900 MHz	Turning radius	> 50 m
Propulsion	Electric, folding propeller	Climb rate	< 3 ms^{-1}
Autopilot	Custom M4	Downlink throughput	> 1500 bytes per second
Control	Auto, operator supervised	Downlink update rate	10 Hz
Power	11 V LiPo, 7600 mAhr	Sensor sampling	up to 800 Hz
Construction	Polypropylene foam	Data storage (on board)	Micro SD card

Table 1. Characteristics of the DH2 sUAS.

Atmospheric
Measurement
Techniques

Open Access

Discussions

Type	Resolution	Accuracy; Range	Time Constant; Cadence	Notes
Hor. Location (GPS)	10 cm	10 m; worldwide	0.2 s; 5 Hz	Real time
Altitude	10 cm	20 cm; -1 km to 20 km MSL	1 ms; 100 Hz	Post flight calibration
Time (GPS)	1 ms	0.2 s; 1 week	0.2 s; 5 Hz	Real time
In-situ temperature	0.1 C	2 C; -60 C to +40 C	5 s; 10 Hz	Real time
Rel. humidity	0.01 %	4 %; 0 % to 100 %	8 s; 10 Hz	Real time
Airspeed	0.05 ms^{-1}	0.2 ms^{-1}; 10 ms^{-1} to 20 ms^{-1}	5 ms; 800 Hz	Post flight calibration
Coldwire temperature	0.003 C	2 C; -60 C to +40 C	0.5 ms; 800 Hz	Post flight calibration
Hotwire velocity	0.01 ms^{-1}	0.2 ms^{-1}, 10 ms^{-1} to 20 ms^{-1}	0.5 ms; 800 Hz	Post flight calibration
C_T^2	10^{-6} m$^{-2/3}$K^2	10^{-5}; 1.0	1 s; 1 Hz	Post flight calibration
ϵ	10^{-7} m^{2}s^{-3}	10^{-6}; 0.1	1 s; 1 Hz	Post flight calibration
2D vector wind	0.001 ms^{-1}	0.5 ms^{-1}; 0 ms^{-1} to 30 ms^{-1}	0.1 s; 1 Hz	Post flight calibration
IR temperature	0.1 C	5 C; -40 C to +40 C	0.1 s; 10 Hz	Real time

Table 2. Sensing Capabilities of the DH2 sUAS.

2.2 Integrated Sounding System (ISS)

An Integrated Sounding System (Parsons et al., 1994) was deployed to monitor the large-scale wind and thermodynamic environment, in close proximity to the UAV measurements. The ISS consisted of a Vaisala MW41 radiosonde sounding system, a LAP3000 915 MHz radar wind profiler, and Lufft WS700/WS800 surface meteorological sensors on a mast at 2 and 10 m. Ninety-three balloon-borne RS41-SGP radiosondes were launched between 3:00 AM and 7:00 AM LT at 30 to 60 min intervals every night, providing five to nine soundings each measurement day.

The ISS automatically ingests surface observations from a set of reference sensors (T/RH, and wind using Lufft WS700 and pressure using Vaisala PTB210) at 1.8 and 3 m. To achieve frequent soundings (< 60 min apart), communications were terminated well before balloon burst (at 12 km) to enable launch preparations for subsequent soundings. The balloon Helium volume was adjusted to achieve a median ascent rate of ~ 3.5 ms^{-1}.

The LAP3000 915 MHz radar wind profiler was operated in a low-height range mode to provide data at 60 m intervals between 200 m to 4.5 km AGL. Due to the dry conditions, winds were measured only up to 2 km on most days. The radar employed five beam directions and raw Doppler spectra were recorded every 30 s. Zonal and meridional wind components were calculated from spectral moments averaged over 30 min.

Time-altitude data from radiosondes and the wind profiler were relayed hourly to the UAS flight deployment team to aid in-flight planning. Examples of ISS observations on 1 November 2017 are shown in Figure 3. Wind profiler data were used to monitor relevant events like precipitation (descending features in signal to noise ratio (SNR)), low-level jets (midnight at $\sim$2 km), KHI (overturning features in the plots - enlarged in the insets of SNR and vertical velocity, e.g. see Figure 3).
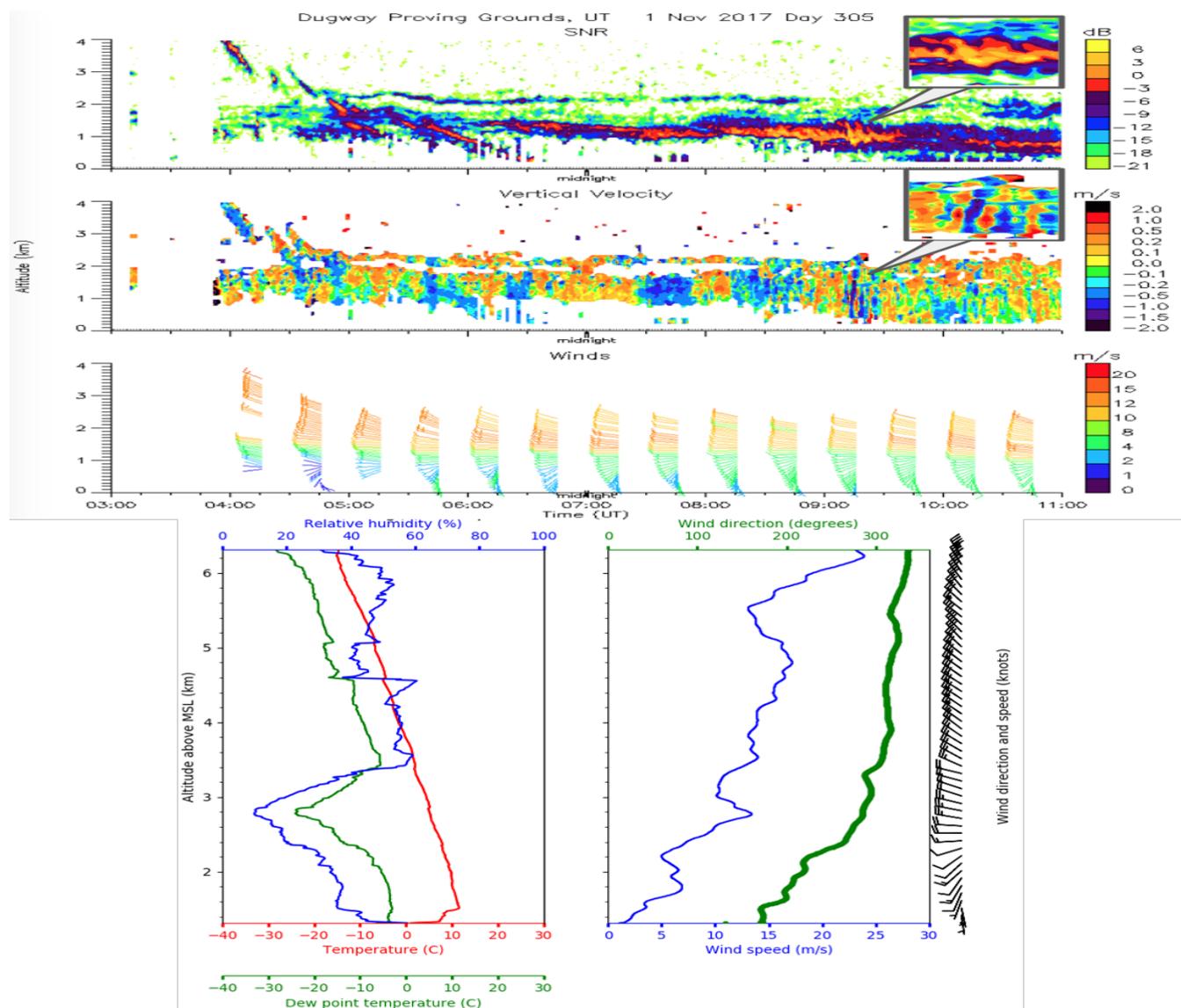
Figure 3. Example measurements by a) the radar wind profiler with SNR (top); vertical velocity (middle; blue/red colors indicate downward/upward motions); and wind barbs (bottom). Insets show enlargements of a 20 min period from 0905-0925 UT. b) The sounding at 0900 UT; red and green lines show temperature and dew point temperature, and the blue line shows relative humidity (left). The horizontal wind speed (blue line) and direction (green line) are shown at right.

2.3 Campaign Meteorological Conditions

Weather forecasts for sUAS flight planning were provided by the DPG Meteorology Division. Weather briefings consisted of
2-day forecasts from the Four-Dimensional Weather System (4DWX), and the most recent observations of surface and upper-level conditions obtained from the DPG MET instrumentation. 4DWX uses the advanced research version of the Weather

Research and Forecasting (WRF) model to predict the weather conditions at the US Army Test and Evaluation Command (ATEC) Ranges (Knievel et al., 2017; Liu et al., 2008). The system is a product of collaboration between ATEC and NCAR. The local surface conditions were obtained using a network of towers that includes 31 SAMS and 50 mini-SAMS. Each

160   SAMS reports 5 min averaged wind speed and direction at 2 m and 10 m, temperature, and relative humidity (T/RH) at 2 m, and precipitation. The mini-SAMS towers provide additional 10 m T/RH measurements with average values reported every minute. Doppler radar wind profilers provided real-time wind profiles from 120 m up to 5 km. The forecasts included expected synoptic-scale patterns, for example, expected times of frontal passage, development of surface inversions, and cloud cover.

During the campaign, DH2s were flown between 2 and 8 AM LT to sample the evolution of nocturnal atmospheric conditions.

165   Weather briefings were provided to the team each day at 0:30 AM, so that launch sites and deployment strategies could be specified based on the most recent information. An example dataset showing 4DWX model predictions of surface temperature and horizontal winds at 0900 UT (2 AM LT) on 6 November 2017 is shown in Figure 4. Figure 5 shows the observed horizontal wind vector from the 449 MHz radar wind profiler on November 6 between 0200 Z and 0800 Z (7:00 PM to 1:00 AM LT). Observed T/RH, and winds from all the soundings throughout the campaign are shown in Figure 6. Conditions were mostly

170   dry with occasional evening precipitation. Surface winds during the first week of the campaign (24 October to 1 November 2017) were consistently strong from the South (see top right panel in Figure 6). Thereafter, surface winds were consistently from the North. The 4DWX model predicted Northerly surface winds in the valley for the last two weeks of the campaign, and the wind forecasts agreed closely with the DPG MET 449 MHz wind profilers. Predicted surface temperatures were between 0 and -5 °C for most nights.
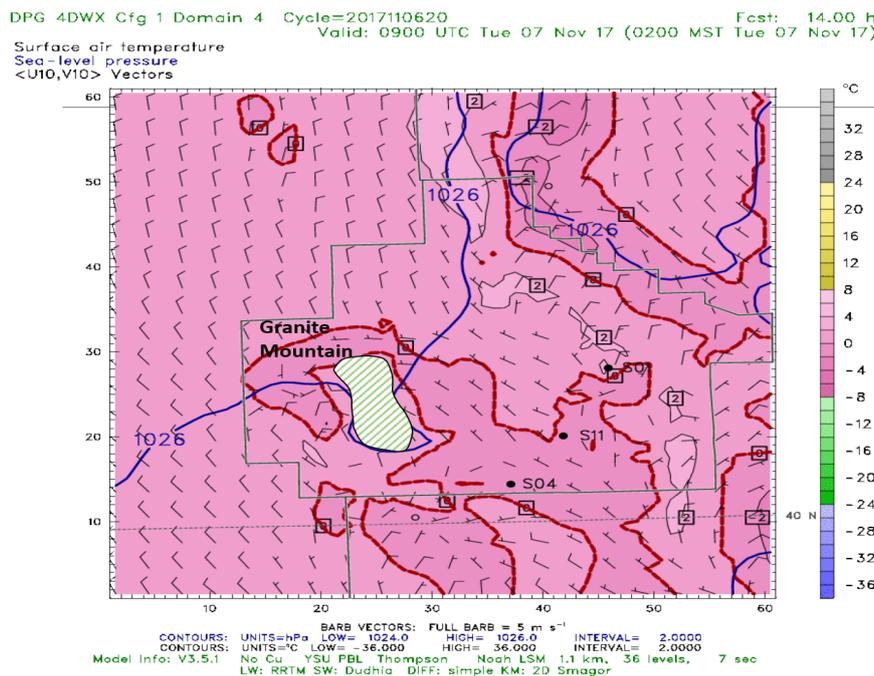

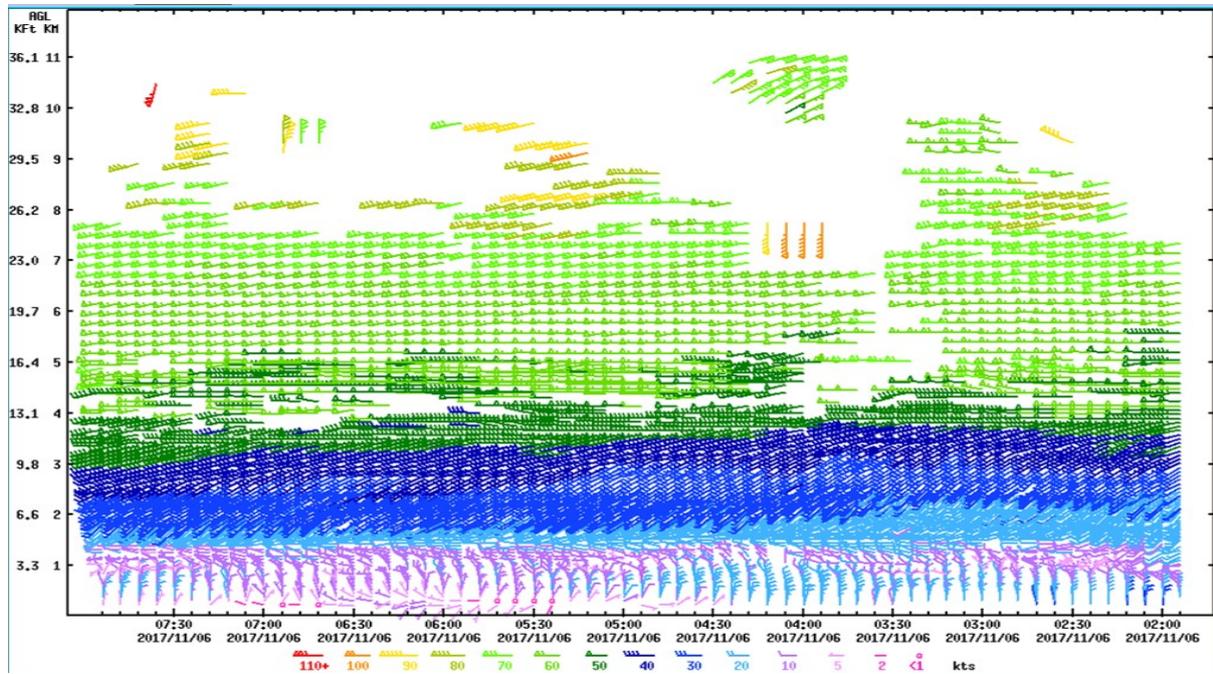**Figure 4.** Example WRF forecast of temperature, wind speed, and direction at 0900 UT (2 AM LT) on 6 November 2017.

Figure 5. Horizontal wind vector measured by the 449 MHz wind profiler between 02 and 08 UT on 6 November 2017.
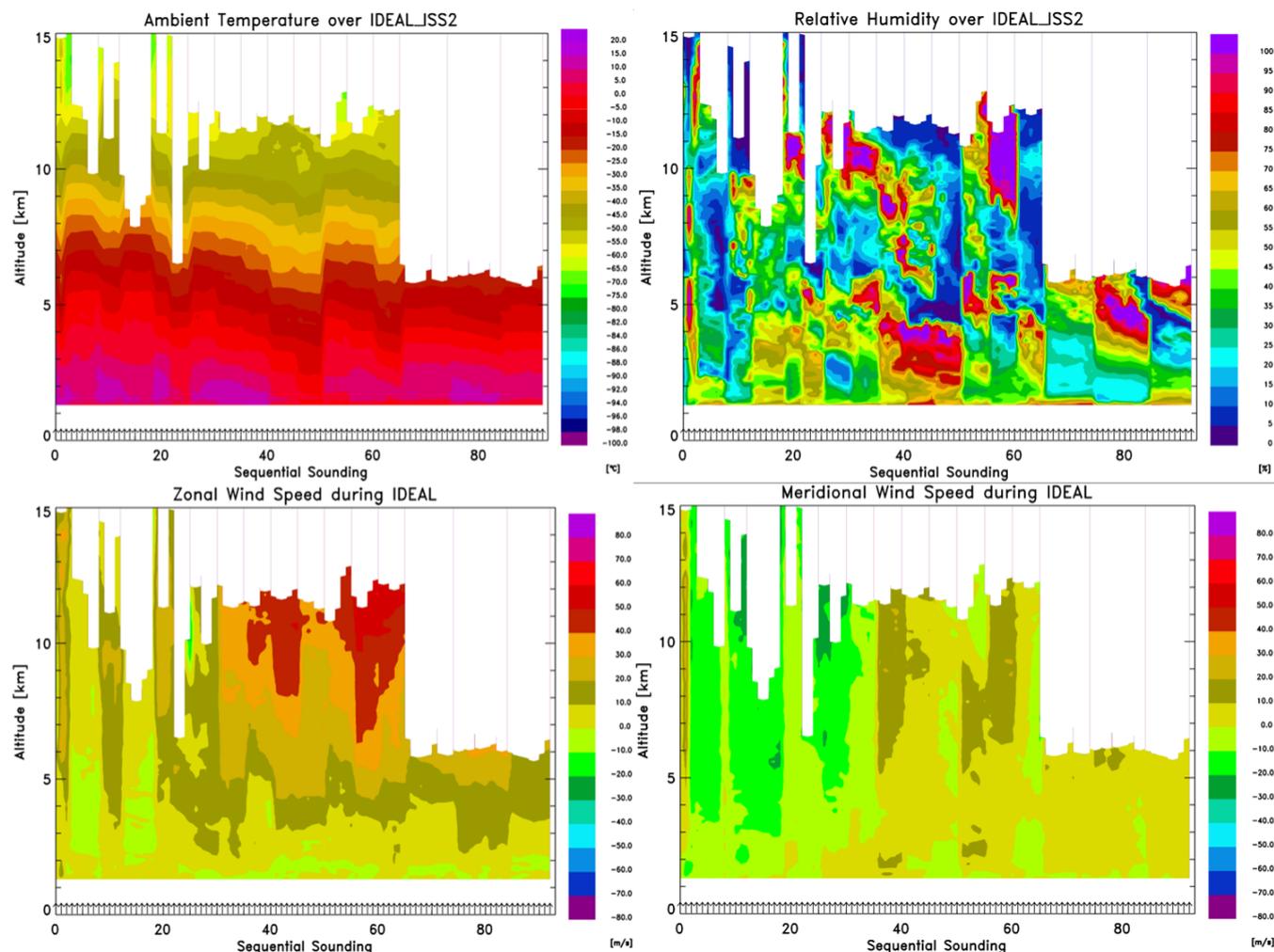
Figure 6. Vertical profiles of temperature (top left), humidity (top right), and zonal and meridional winds (bottom, left and right) measured by all radiosonde launches. Note: communications with some sondes were terminated early to facilitate a faster launch cadence.

175   The stable nocturnal boundary layer was shallow on most nights (~ 75 m), but occasionally increased to 200 m. Directional shear was frequently observed between the surface and altitude of 2 km. A weak westerly nocturnal jet was often observed at 2 km. Strong speed shears observed above 2 km occasionally resulted in KHI as shown in the insets of signal to noise ratio (SNR) and winds (top tile) in Figure 3. The background atmosphere was statically stable ($N^2 > 0$) on most nights, with occurrences of stability and humidity sheets at various altitudes separated by weak, intermittent, and sporadic turbulence events.

3   Observational Strategy

The IDEAL measurement program was designed to take advantage of the high-spatial resolution, range, and dexterity of DH2 aircraft to provide high-resolution in-situ observations of S&L structures and their evolution under stable boundary layer and lower troposphere conditions. The low cost and ease of operation of DH2 sUAS, discussed in Section 2.1, enabled simultaneous, multi-path measurements intended to quantify local S&L flow evolution, scales, and the dynamics underlying their small-scale structures. Because in-situ measurements are necessarily sparse, DH2 trajectories were designed to provide successive, multiple-DH2 sampling of local flows along horizontal, inclined, and spiraling vertical flight paths sampling common volumes over tens of minutes.

Flight planning relied significantly on 4DWX weather forecasts and local ISS and SAMS measurements described in Section 2.2. Evolution of predicted winds and the thermodynamic state of the synoptic-scale flow were used to identify the likely most favorable site for DH2 measurements each day. The two flight operation locations (marked 'Flight Site 1' (FS1) and 'Flight Site 2' (FS2) in Figure 1) were located on the eastern flank of Granite Peak and in the central portion of the valley, respectively. FS1 and FS2 were chosen to be upwind of the ISS deployment site for two different wind conditions. Flight operations were conducted from FS1 on days when the predicted surface winds were from the west, and the forcing was at least as strong as $8 \, \mathrm{ms^{-1}}$ to $10 \, \mathrm{ms^{-1}}$. This maximized the likelihood of observing mountain wave influences on S&L structures due to Granite Peak at FS1, and accompanying fine-structure interactions leading to S&L dynamics. Flight operations were conducted from FS2 on days when the predicted winds were from the south and relatively weak.

Most recent radiosonde winds and temperatures guided the choice of measurement location and characterized the S&L structures at coarse vertical resolution. An example of the real-time radiosonde data relayed to the measurement team on 6 November 2017 is shown in Figure 7. Periodic soundings monitored the spatial variability, intermittency, and temporal evolution of the layered structures at coarse vertical resolution and contributed to go/no-go decisions for DH2 flight sorties based on the prospects for encountering interesting dynamics while avoiding high-wind conditions.
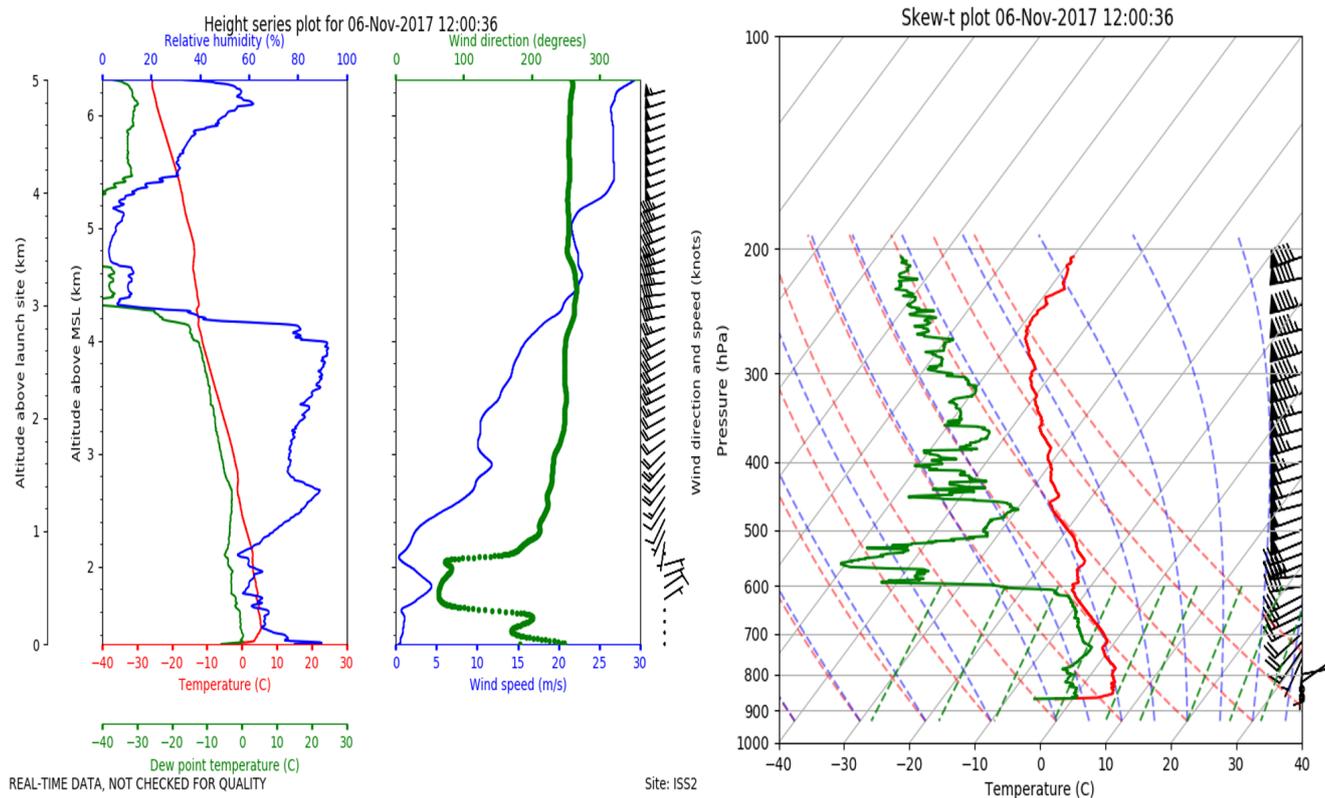
Figure 7. a) Horizontal wind speed, direction, and temperature profiles from the radiosonde launch at 00 UT on 6 November 2017. b) The pressure-temperature profile (red – temp., green – dew point temp.) and the horizontal wind hodograph.

Figures 8 and 9 depict typical DH2 sortie composed of three simultaneous flights: a dedicated sounding DH2 (A1 in Figures 8 and 9) to characterize the local vertical structure above the launch location, and two aircraft (A2 and A3 in Figure 8 and 9) intended to characterize the horizontal structure and evolution of S&L structures at specific altitudes identified by A1. A1 in

205 each sortie sampled in a helical flight pattern (100 m radius, 2 ms^{-1} ascent/descent rate) and telemetered real-time θ, T/RH, and aircraft altitude (among other parameters) to the ground station. This information was used to identify target altitudes for aircraft A2 and A3 launched a few minutes later. A2 and A3 typically flew in horizontally elongated "racetrack" patterns up to about 1.5 km in length, oriented along the flow stream direction to observe lateral variability of the S&L structures.
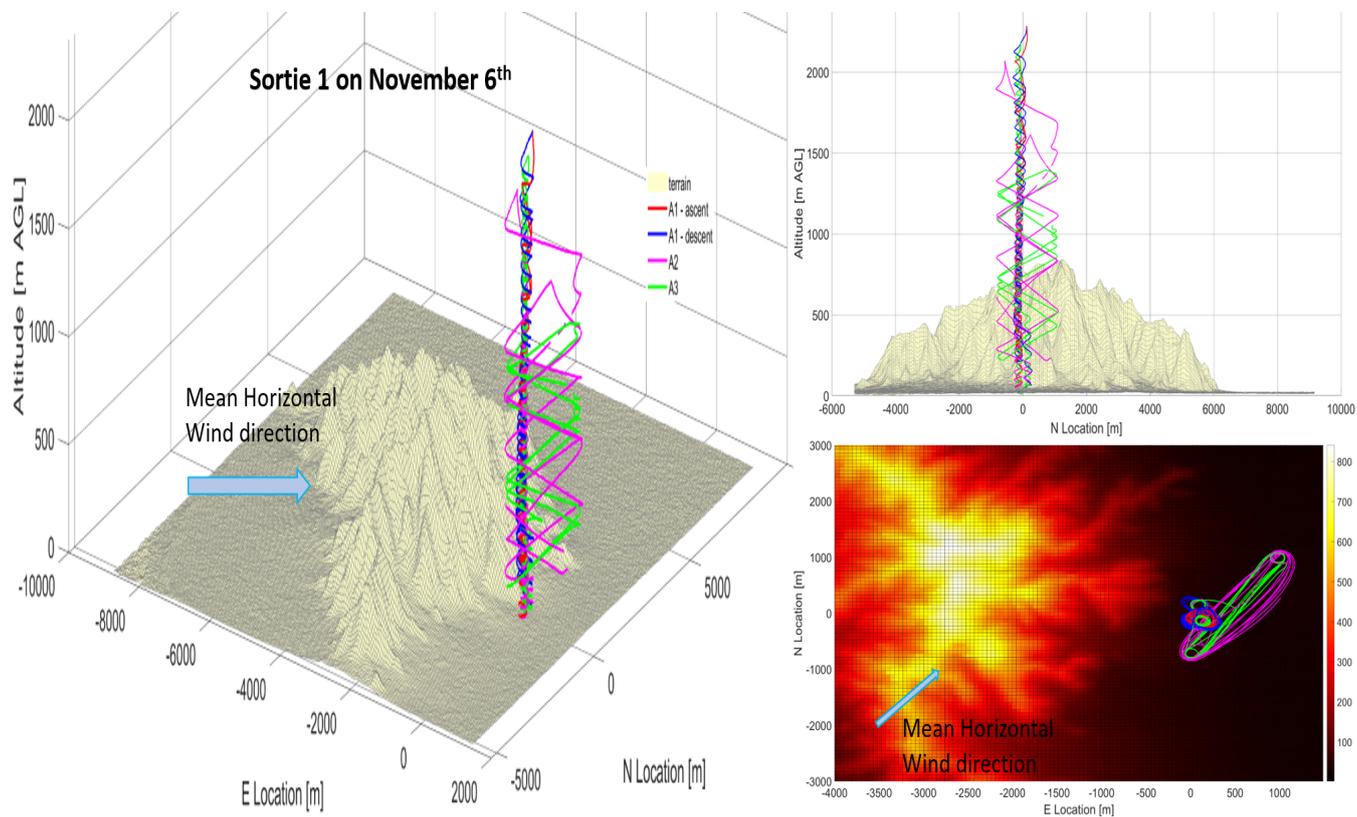
Figure 8. (Left and top right panels) Plots depicting the trajectories of the three aircraft A1, A2, and A3 from FS1 during sortie 1 on 6 November 2017. The low-relief terrain feature is Granite Peak (standing 850 m above the surrounding planes). (Bottom Right panel) Horizontal map showing Granite Peak with mean wind and sUAS trajectories.
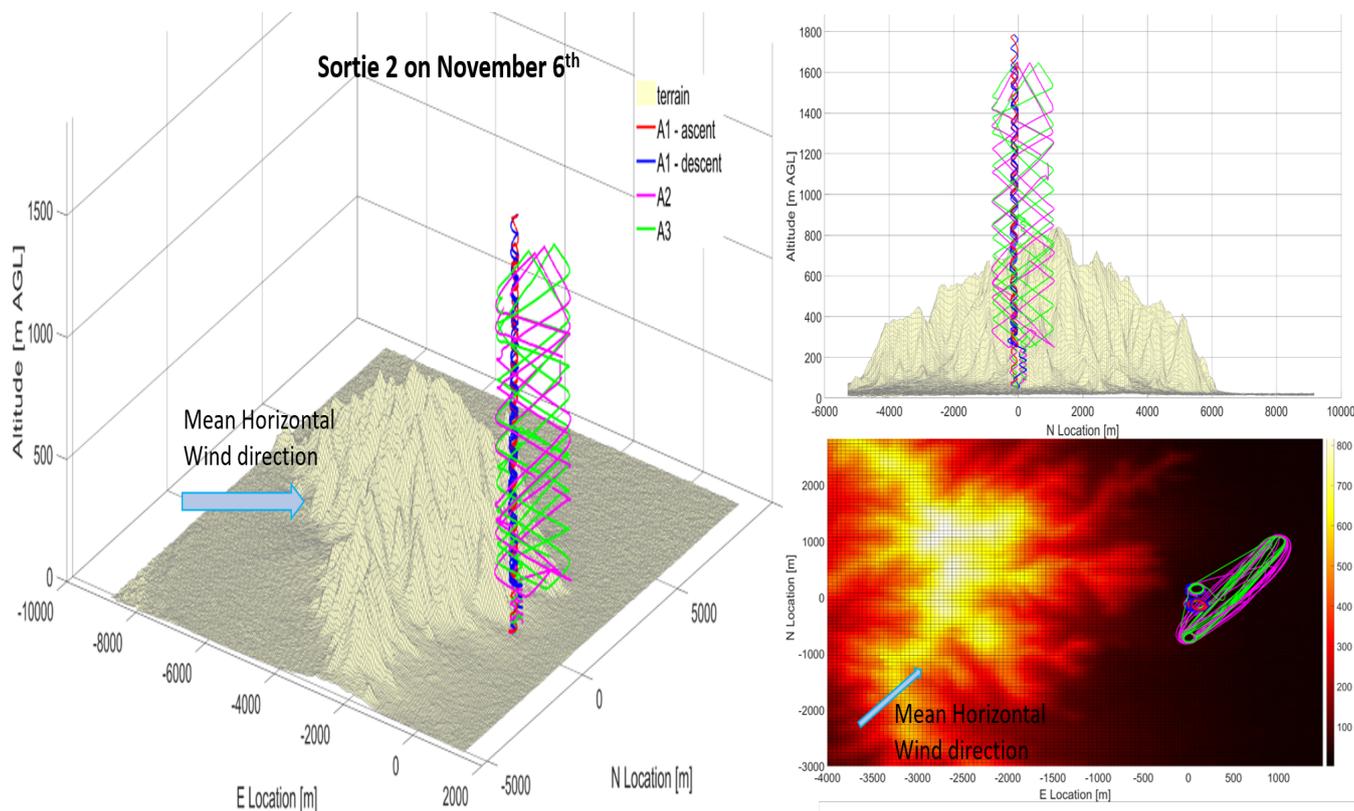
Atmospheric
Measurement
Techniques
Discussions

Figure 9. Trajectories of the three aircraft A1, A2, and A3 from Sortie 2 on 6 November 2017.

A total of 14 flight sorties from FS1 and 13 sorties from FS2 were performed. Most of these involved three simultaneous

210 DH2 flights. Each sortie had one vertical "sounding" aircraft A1. Trajectories of the other "lateral" aircraft varied significantly, depending on the conditions relayed by recent radiosonde data and on the conditions observed by A1. Some of these lateral trajectories concentrated on a particular turbulent layer evolution, moving laterally while slowly ascending and descending through a narrow altitude range to observe spatial and temporal variability in the layer. Other sorties, e.g., as shown in Figure 10, sought to investigate temporal evolution of multiple layers with measurements that were displaced evenly in time. The

215 overview plots of T/RH, static pressure, wind speed and direction, 3D GPS position, and velocity data along with the flight notes for each sortie are available for download on the IDEAL project preliminary analysis web page hosted by the University of Colorado (see Section 5).
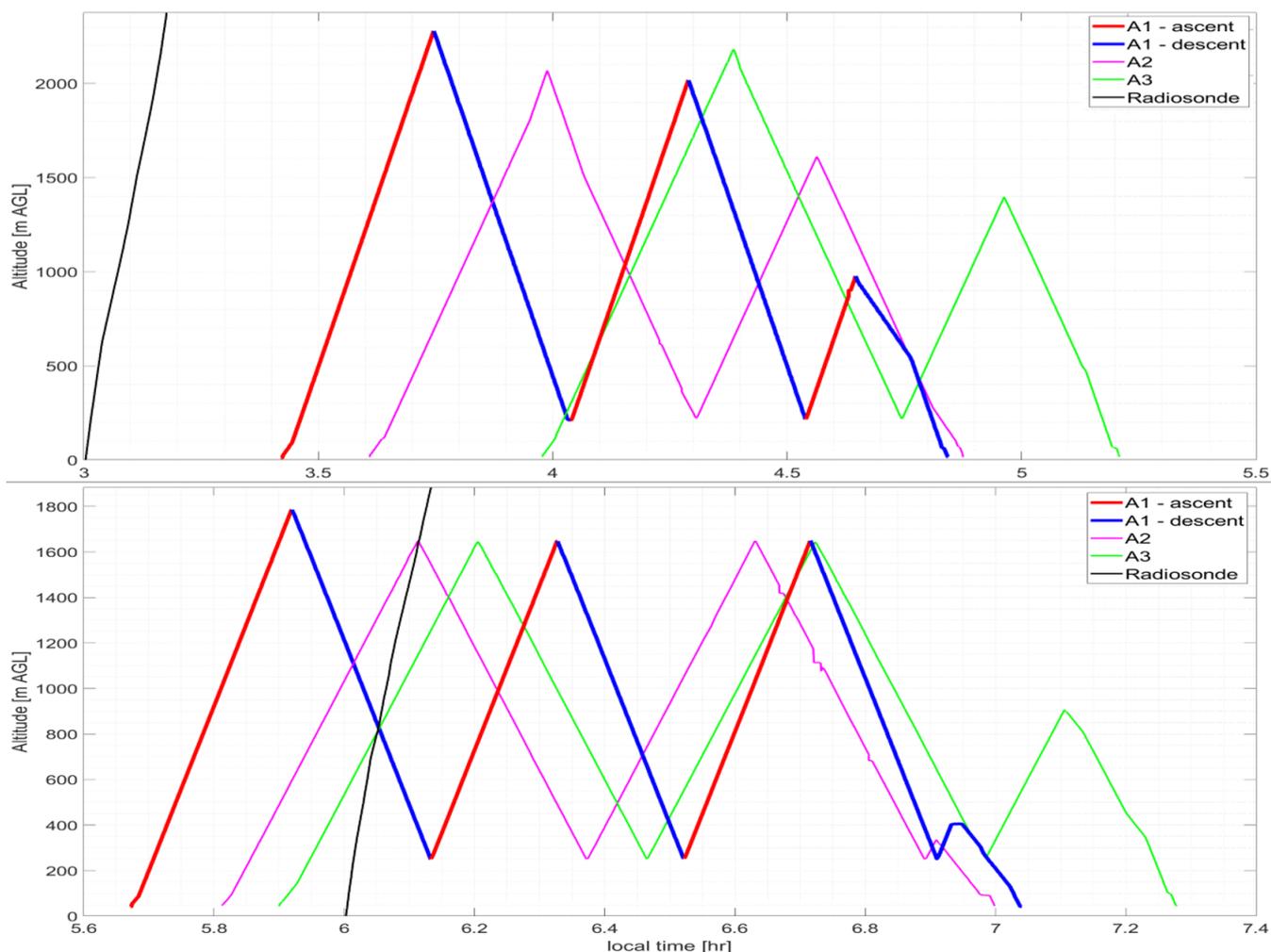
Figure 10. Time series showing altitude vs time for the two DH2 sorties on 6 November. (top: Sortie 1, bottom: Sortie 2), along with coordinated radiosonde trajectories (black lines). The plot shows co-ordination between the three DH2 launches (red-blue, green, and magenta lines) and the radiosonde sounding (black line).

4 Preliminary Data Analysis and Findings

DH2 identified 58 individual stable sheet structures roughly 25 to 50 m deep from the measurements of 31 multi-aircraft flight sorties (72 individual flights). Stability ducts, consisting of large N^2 sheets constraining weakly stable and weakly turbulent layers as deep as 400 m, were frequently prevalent. Such structures, often persisting up to five hours under very stable conditions, were commonly observed at the peak altitude of Granite Peak (850 to 900 m AGL). Altitude undulations in persisting stable structures during strong (8 to 10 ms^{-1}) eastward-wind forcing over Granite Peak suggest the presence

of mountain waves. Temperature gradients as steep as 0.18 Km^{-1} or $\sim 18\Gamma$ (with tropospheric dry adiabatic lapse rate $\Gamma \sim$
225 $9.8 \times 10^{-3} \ \mathrm{Km}^{-1}$) were typically observed across most sheets (see enlarged inset on Figure 12).

One particular case is presented through Figures 11 to 14, exhibiting altitude profiles of measured and derived parameters from spiraling aircraft in two consecutive DH2 sorties (Sorties 1 and 2 at approximately 03 and 05 LT) on 6 November 2017 performed at FS1. The stable nocturnal boundary layer extended to 200 m, and was capped by an inversion layer at these times. Eastward winds aloft up to 12 ms^{-1} were observed. A strong speed shear developed between 1200 and 1600 m AGL.
230 The background atmospheric column was near-neutrally stable ($N^2 = 10^{-5} s^{-2}$). The DH2 observed an undulating sheet in the measurements of temperature and humidity at 800 m and another sheet formation at 1300 m. An intermittent patch of weak turbulence, 200 m deep, was observed between 1450 and 1650 m. The high-resolution (3 m vertical) profiles of ϵ and C_T^2 in Figures 12 (from S1 at 03 LT) and 14 (from S2 at 05 LT) exhibit signs of diminishing turbulence likely leading to re-laminarization enabling formation of a steep temperature gradient that is characteristic of a highly stable sheet: the extinction
235 of turbulence is apparent in the abrupt reduction of ϵ just below 1400 m from the first ascent to the first decent in Figure 14. The confined elevation of C_T^2 immediately below 1400 m in Figure 14 further supports this conclusion.
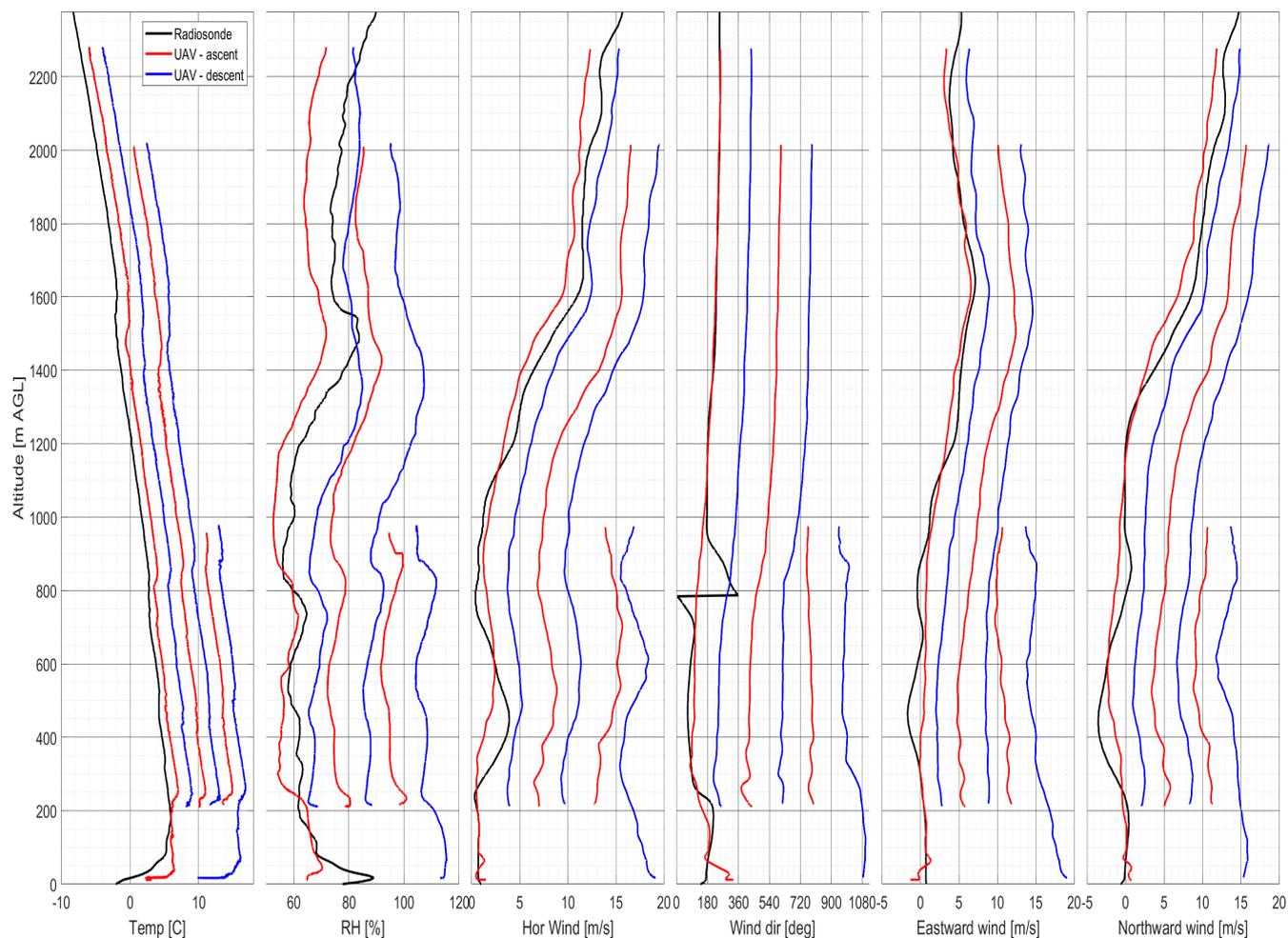
Figure 11. Vertical profiles (offset for clarity) of temperature (offset: 2 C), humidity (offset: 10%), horizontal wind speed (offset: $3 \, \mathrm{ms}^{-1}$) and direction (offset: $180°$), eastward and northward winds (offset: $3 \, \mathrm{ms}^{-1}$) from the profiling aircraft in S1 on 6 November 2017. Red (blue) lines indicate ascending (descending) flight legs.
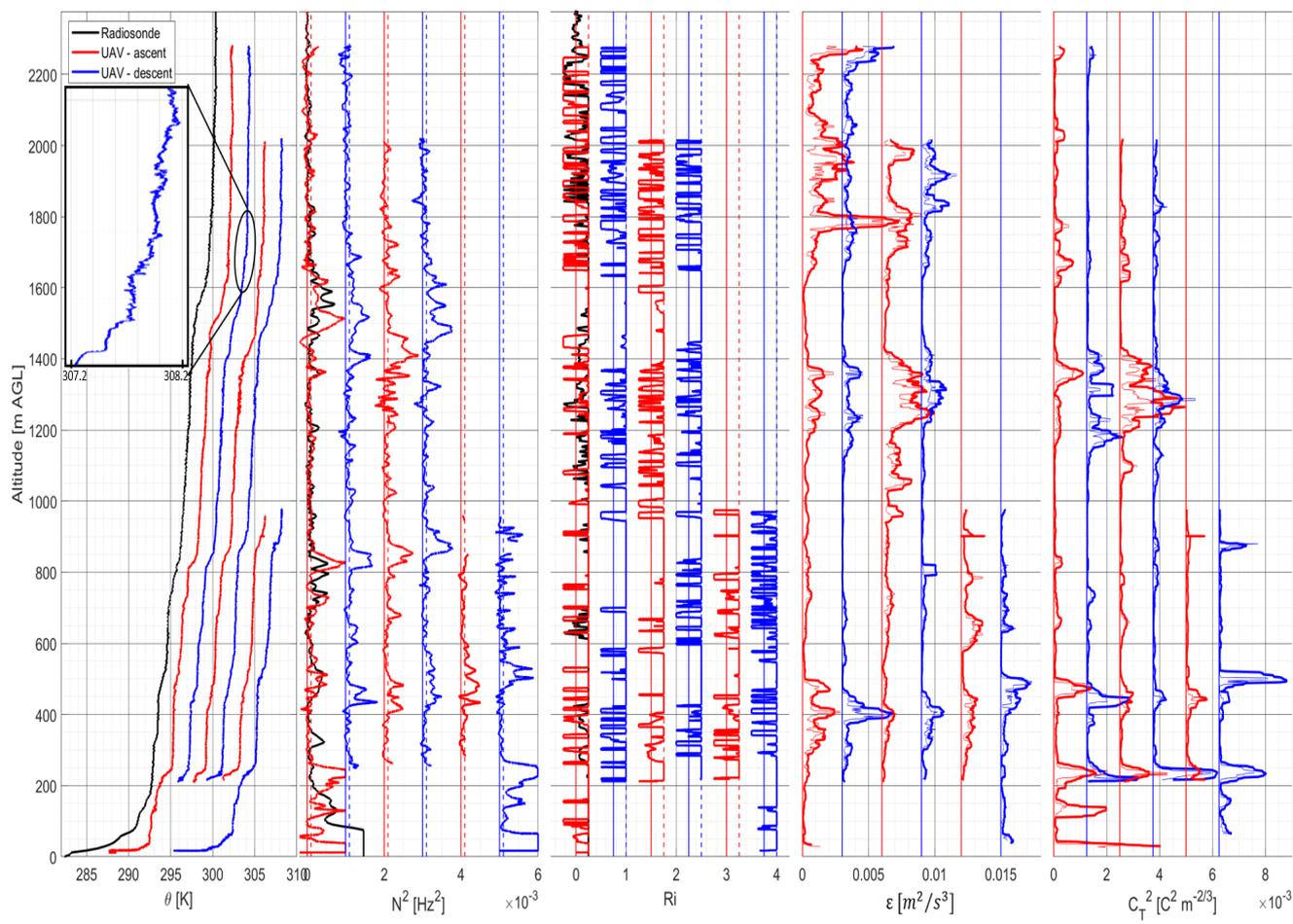
Figure 12. Vertical profiles (offset for clarity) of θ (offset: 2 K), N (offset: 10^{-3} s^{-2}, dash line: $N^2 = 10^{-4}$ s^{-2}), Ri (offset: 0.75, dash line: $Ri = 0.25$), ϵ (offset: 3×10^{-3} m^{2}s^3), and C_T^2 (offset: 1.25×10^{-3} C^{2}m$^{-2/3}$) from the profiling aircraft in S1 on 6 November 2017.
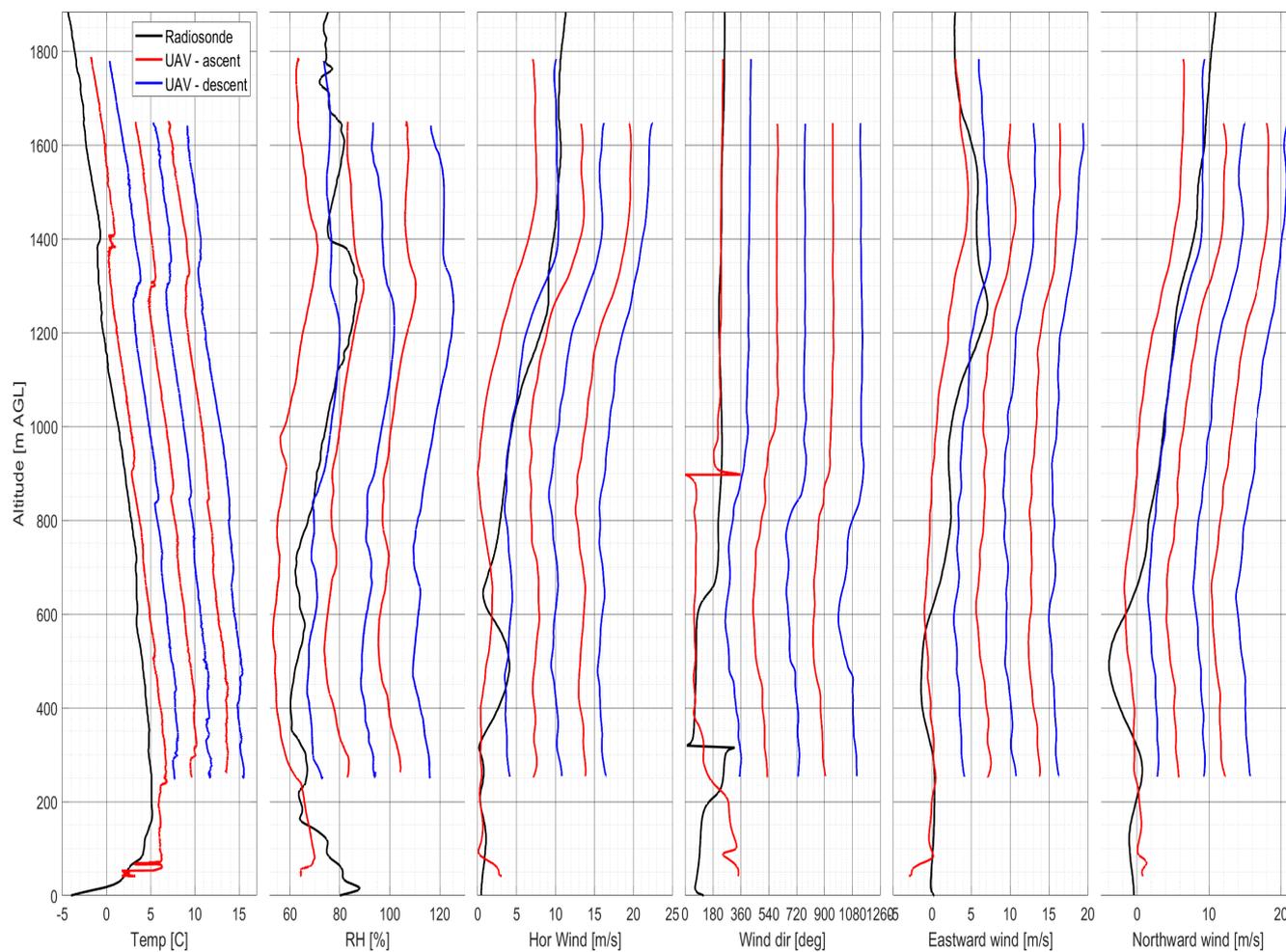
Figure 13. Vertical profiles of Temperature, Humidity, horizontal wind speed and direction, Eastward and Northward Winds from the vertically sampling aircraft in S2 on 6 November 2017.

Atmospheric
Measurement
Techniques
Discussions

Open Access

EGU
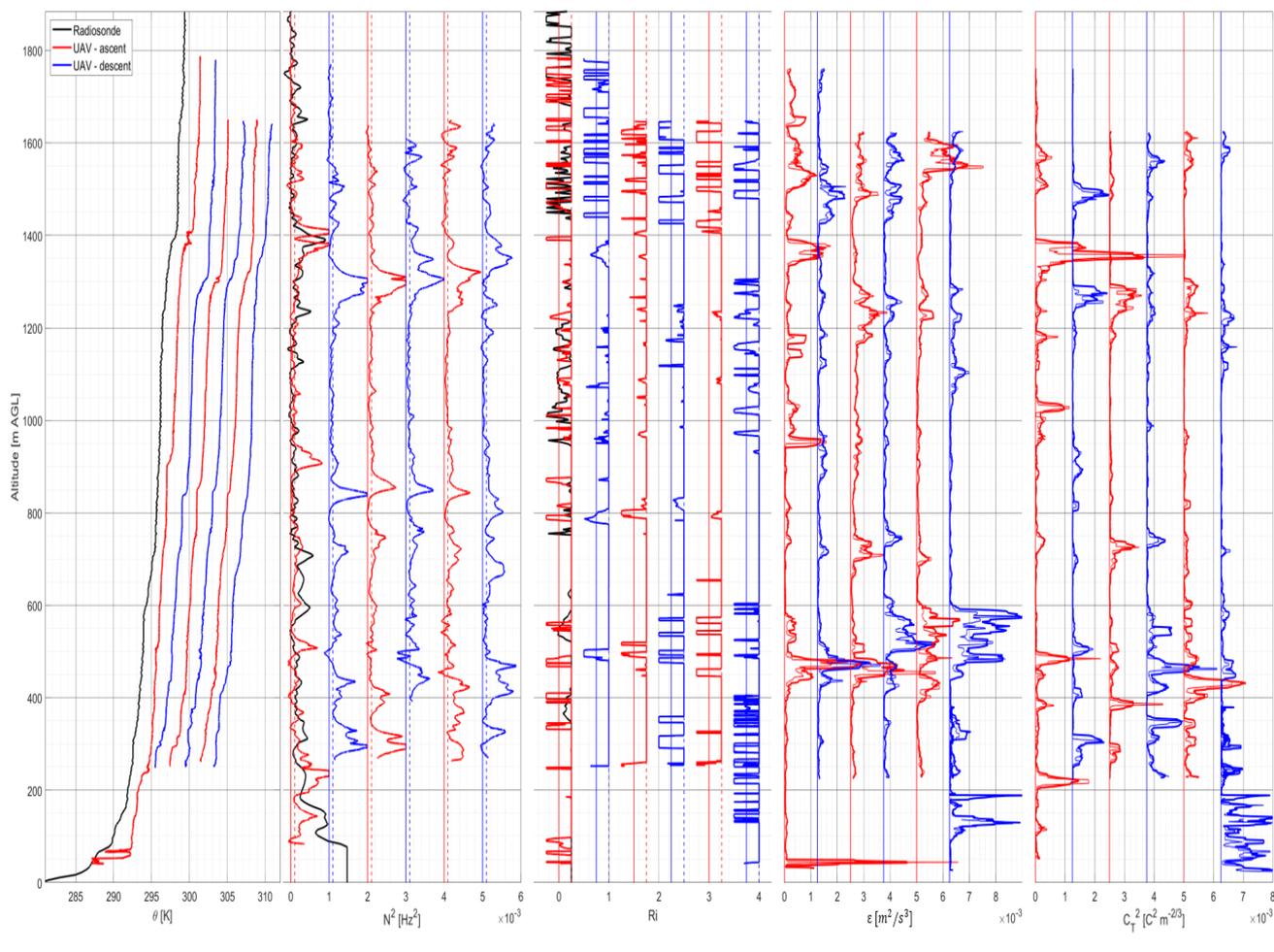
Figure 14. Vertical profiles of Potential temperature, Buoyancy frequency, Gradient Richardson Number, TKE dissipation rate (offset: 1.25×10^{-3} $\mathrm{m^2 s^{-3}}$), and temperature structure function from the vertically sampling aircraft in S2 on 6 November 2017.

Figures 15 and 16 show plots of the measured and estimated parameters from radiosonde soundings monitoring the atmospheric column at the ISS location (9.5 km downstream of FS1) on 6 November 2017. The potential temperature and humidity profiles from these periodic soundings suggest that the two sheets observed by DH2 at FS1, shown in Figures 11 and 12 (at 800 m and 1300 m), are highly localized and likely decay as they advect. The oscillating motion exhibited by the sheets suggests weak wave activity in the leeward side of Granite Peak as a consequence of strong eastward wind forcing. Preliminarily, this case seems to align well with the analysis presented in Tjernström et al. (2009) and Balsley et al. (2018) implying that S&L structures are maintained by GW-FS interactions.

A shallow nocturnal boundary layer (200 m deep), recurring sheet activity at the mountain top (850 m) and aloft (1450 - 1600 m) separated by deep, intermittent turbulent layers (600 - 800 m deep) was the general theme underlying the observations

at FS1. Escalation of shear at altitudes coincidental with the undulating sheet pairs probably destabilized the sheets causing them to decay, and sustain turbulence inside the layers. Detailed analysis of the measurements made by horizontally sampling DH2 (A2 and A3 aircraft from each sortie) is expected to provide insights on the lateral structure and variability of S&L, but limited information on the formation mechanism. However, DH2 measurements provide qualitative information regarding

250   background structure (stability and temperature gradients) and forcing conditions (winds) invaluable for initializing idealised model simulations of such complex dynamics.
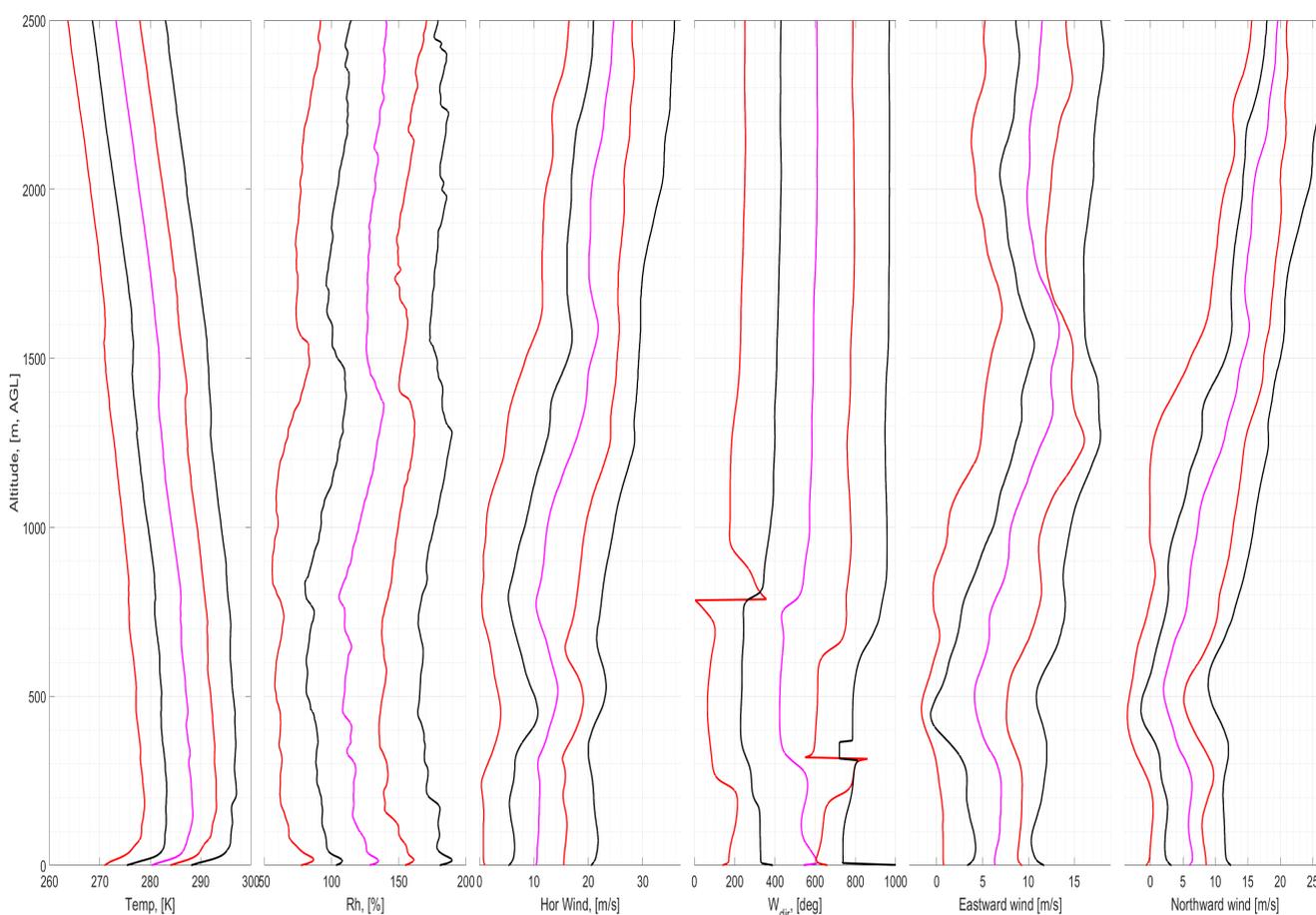
Figure 15. Height plots of Temperature (offset: 5 C), Humidity (offset: 25%), horizontal wind speed (offset: 5 ms^{-1}) and direction (offset: $1800\,°$), Eastward and Northward Winds (offset: 3 ms^{-1}) from five hourly radiosonde launches between 03:00 and 07:00 LT on 6 November 2017.
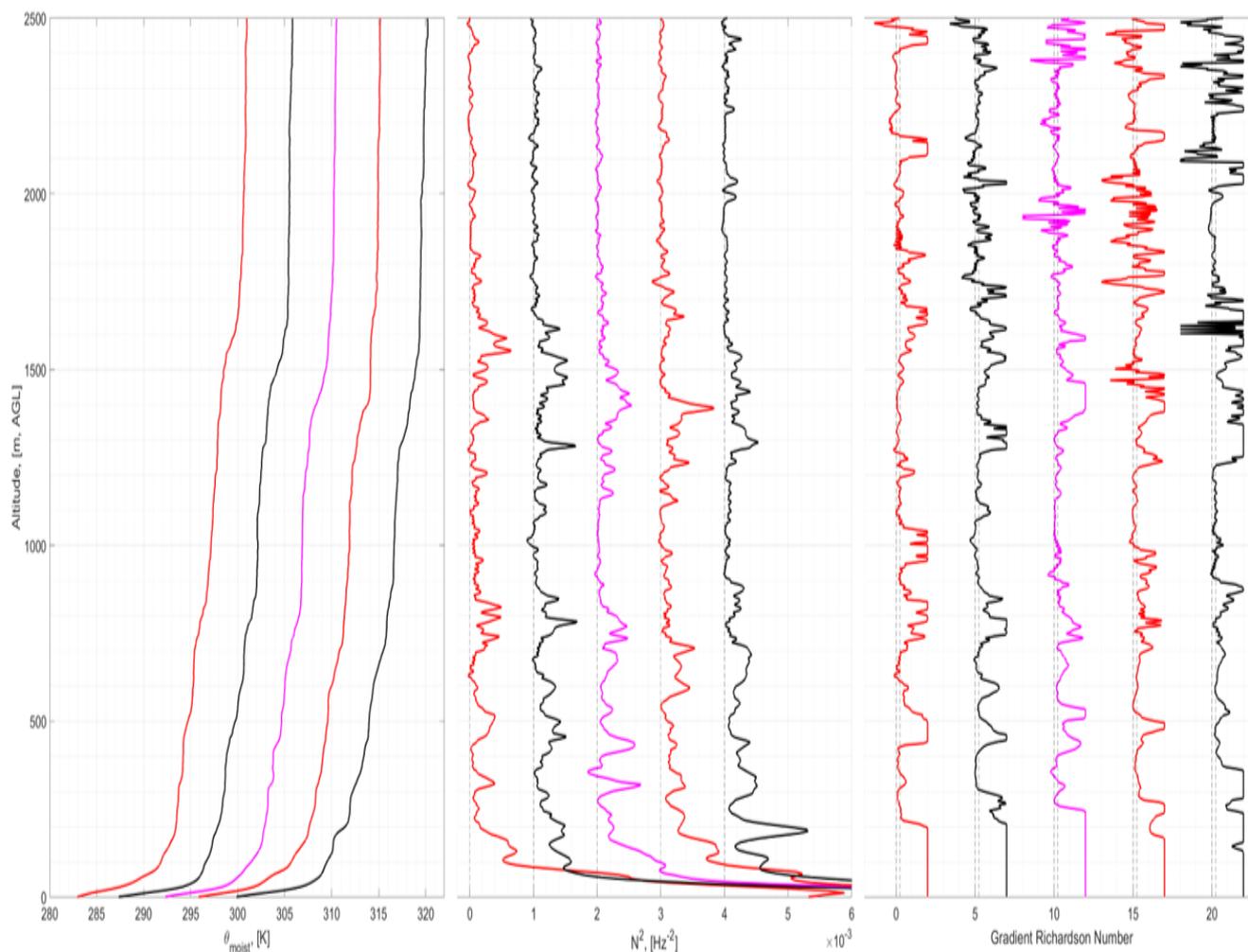
Figure 16. Height plots of Potential temperature (offset: 5 K), Buoyancy Frequency (offset: 10^{-3} s^{-2}) and Gradient Richardson Number (offset: 5, dash line: Ri = 0.25) estimates from five hourly radiosonde launches between 03:00 and 07:00 LT on 6 November 2017.

5 DNS Modeling Supporting IDEAL Planning, Measurements, and Analyses

Initial exploration of formation mechanisms of S&L structures arising from imposed superpositions of convectively stable GWs and dynamically stable mean shears, referred to as multi-scale dynamics (MSD), employed idealized high resolution DNS (Balsley et al., 2018; Fritts et al., 2009b; Fritts and Wang, 2013; Fritts et al., 2013). These DNS simulations revealed a diversity of secondary instability dynamics exhibiting small-scale versions of larger-scale dynamics accompanying more idealized GW breaking and KHI shear instability events. Importantly, multiple examples of these induced dynamics closely resembled small-scale instabilities in high-resolution atmospheric imaging at higher altitudes (Miller et al., 2015; Fritts et al., 2017, 2019; Geach et al., 2020; Hecht et al., 2021), confirming the ability of these DNS to describe both idealized and MSD

Atmospheric
Measurement
Techniques
Discussions

Open Access
EGU

260   instability dynamics. While highly idealized, the MSD also predicted the emergence of these dynamics within induced S&L

structures that emerged from the idealized initial conditions. These initial DNS results, and the emerging DH2 measurement

capabilities, provided the motivations for the IDEAL program, and expanded such MSD studies are contributing to exploration

of the implications of IDEAL measurements.

The DNS of MSD featured a single initial monochromatic GW having an amplitude of $a = (d\theta/dz)_{min}/(d\theta/dz) = 0.5$

265   and an intrinsic frequency $\omega = N/10$. A constant mean stability N, and $Re = 50000$ was assumed to enable instabilities and

turbulence structures accompanying GW-FS dynamics that extend to very small-scales (Balsley et al., 2018; Fritts and Wang,

2013; Fritts et al., 2013). Example fields from the MSD are shown with (x, z) cross sections at the spanwise domain center at

two times separated by $1.5T_b$, for buoyancy period T_b, in Figure 17, left and right. The upper and lower panels show $log_{10}\epsilon$

and N^2, respectively. Red arrows identify KHI progressing from right to left along the most highly-stratified vortex sheet

270   initiated by a GW propagating from right to left and elevating the vortex sheet accompanying its most upward displacement.

Counter-intuitively, the strongest KHI arise at the most stable N^2 because emerging large N^2 arise due to vertical convergence

of the flow, and of the local shear, dU/dz, causing the local Richardson number, $Ri = N^2/(dU/dz)^2$, to decrease below 0.25

because N^2 increases linearly, but $(dU/dz)^2$ increases quadratically with vertical convergence, thus yielding the minimum Ri

at the maximum N^2. Importantly, the $log_{10}\epsilon$ fields reveal that MSD KHI make comparable, or larger, contributions to total ϵ at

275   these times.

An additional DNS designed to explore KHI MSD in environments allowing mis-aligned initial KHI along their axes in

the absence of GW modulations of the initial shear layer was carried out. This DNS was carried out at $Re = 5000$, minimum

$Ri = 0.1$ and employed an initial noise spectrum that led to several cases of "tube and knot" (T&K) dynamics that were

examined in detail by Fritts et al. (2021a) and Fritts et al. (2021b). Figure 18 shows (x,y) and (x,z) planes of $log_{10}\epsilon$ spanning

280     $1T_b$. Two interesting sites within the DNS model domain were examined in detail: one at the spanwise location denoted "a" at

top and bottom in Figure 18 containing two vortex tubes linking to a common KH billow core, and a second at the spanwise

location denoted "b" exhibiting a single vortex tube linking two adjacent billow cores.

Both of these T&K dynamics lead to significantly accelerated transitions to, and enhanced turbulence relative to regions

exhibiting turbulence transitions in the absence of T&K dynamics. See, for example, the rapid expansion of intensifying $log_{10}\epsilon$

285   in the central region, and to the upper left and lower right of the central billow core, around location "a" at successive times at

top in Figure 18. Corresponding vertical cross sections along "a" in the center row at bottom in Figure 18 reveal that the vortex

tubes either side of the central KH billow drive its more rapid breakdown to turbulence relative to the other locations shown.

Related, but less aggressive, T&K dynamics also accompany the single vortex tube linking adjacent KH billow cores at left

and center at location "b" at top in Figure 18. These T&K dynamics are likewise more aggressive than in their absence; see the

290   advanced transitions to turbulence at this location (site "b" in the bottom row at bottom in Figure 18) relative to that in the top

row exhibiting no T&K dynamics.

The expected wide-spread presence of such dynamics, given the highly-modulated local sheared environments in which they

arise, such as seen to arise in Figure 17 from initially two-dimensional initial conditions, suggest that KHI T&K dynamics in

the atmosphere are more the rule than the exception, and were likely major contributors to the small-scale dynamics and S&L

295 structures measured during the IDEAL field program.

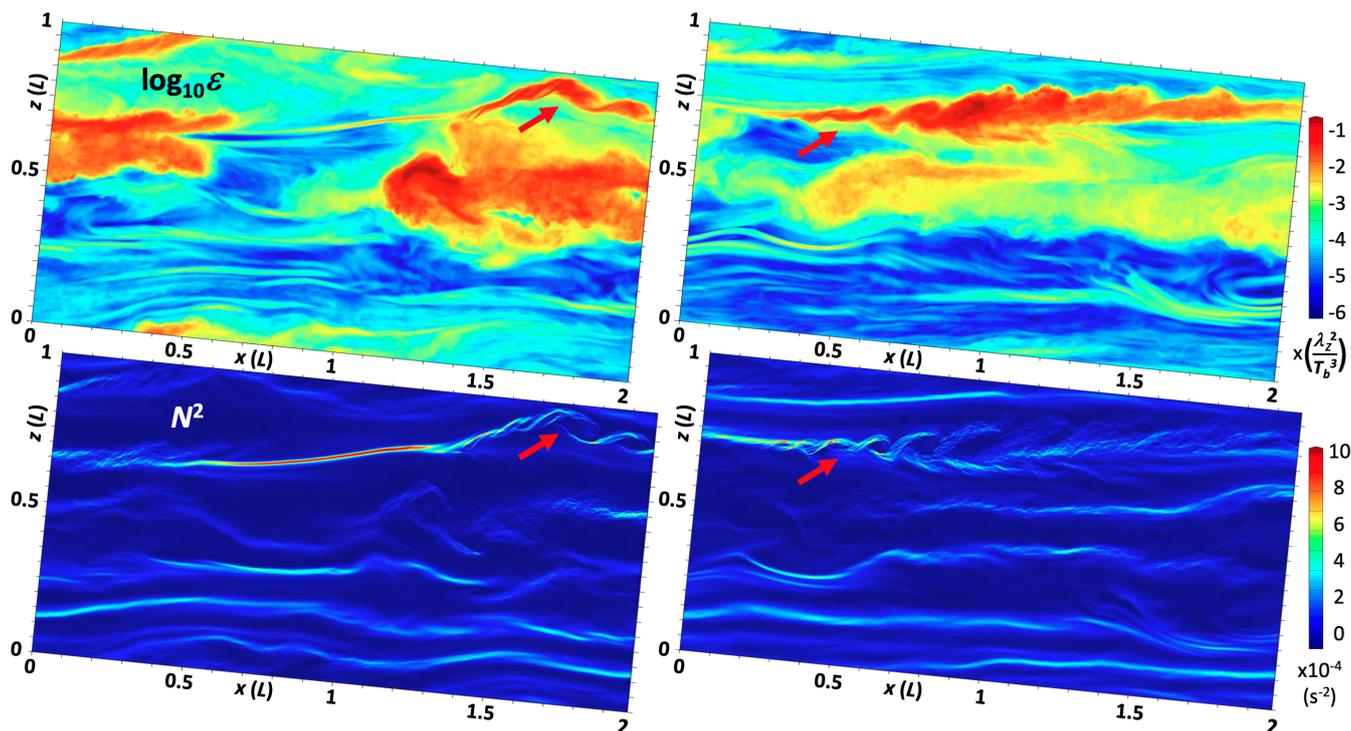**Figure 17.** $log_{10}\epsilon(x,z)$ (top frames) and corresponding $N^2(x,z)$ (bottom frames) evolution at $y=0$. The two set of frames presented here are $1.5T_b$ apart in time.
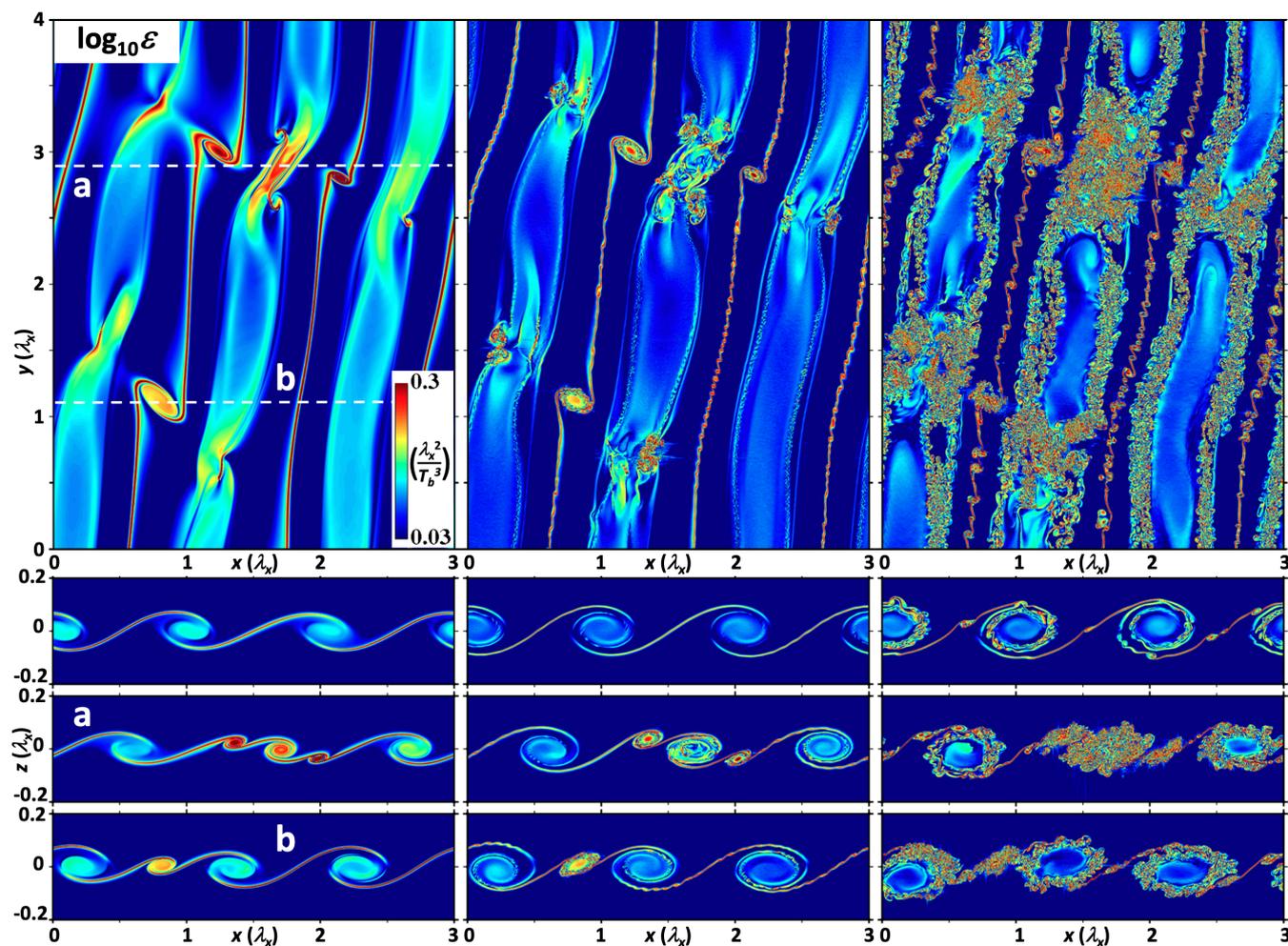
Figure 18. (x,y) and (x,z) cross sections (at $z = 0$ and $y = 0$) of $log_{10}\epsilon$ spanning $1T_b$. The top panels, showing (x,y) planes, depict the evolution of vortex tubes at locations "a" and "b". The bottom panels show (x,z) cross sections at $y/L = 2$, "a", and "b" locations.

6 Conclusions and Future work

In this overview, we have presented the goals and the observational strategy of IDEAL program. The sensors and platforms used have been described in detail. An example has been provided using data from Sorties 1 and 2 on 6 November 2017. The example clearly shows the evolution of S&L structures in the lower atmosphere.

300   So far, only the data from the vertical sounding aircraft (A1) in each IDEAL sortie have been analyzed. Much remains to be done. Further work using data from the vertical sampling flights is underway for identifying critical wave parameters to aid in the DNS studies. The analysis, interpretation, and visualization of sUAS sampling along horizontal slant path trajectories present primary challenges in characterizing the lateral structure. Analysis presented in Balsley et al. (2018) considers Data-

Atmospheric
Measurement
Techniques
Discussions

Open Access

EGU

305 Hawk measurements on a slant path by sampling single point slant path trajectories of DNS model outputs to make realistic comparisons between the observed and simulated data. A similar resampling strategy is expected to be employed to interpret the slant-path flight data from IDEAL campaign.

Appendix A: Data Access

Summary plots as portrayed in Figures 11 to 14 (along with other preliminary analysis data, relevant flight notes and flight metadata) for each sUAS sortie are available for download through the IDEAL preliminary analysis website hosted by the

310 University of Colorado at https://www.colorado.edu/p129765c7060/home. The observational data from sUAS, ISS soundings and 915 MHz radar wind profiles, DPG 449 MHz radar wind profiles, SAMS, mini SAMS and ancillary data are available for download on request at https://www.eol.ucar.edu/field_projects/ideal in standard binary formats (.netcdf and .mat). Documents describing processing and quality control for all the platforms along with the metadata files are made available with the datasets.

Author contributions.

320 DL developed the DH2 sUAS vehicles and AD assisted in developing and testing the sensing systems, DL led the DH2 portion of the field campaign and AD assisted in DH2 deployment. AD and DL carried out the preliminary DH2 data analysis. WB led the ISS siting, operation, and data handling activities, and DZ hosted the campaign at DPG, including coordination of daily weather briefings. DF and LK provided remote science guidance during the campaign. DF led the related DNS modeling studies supported by LW and TL.

Competing interests.

325 The authors have no competing interests regarding this work.

References

Balsley, B. B., Frehlich, R. G., Jensen, M. L., Meillier, Y., and Muschinski, A.: Extreme Gradients in the Nocturnal Boundary Layer: Structure, Evolution, and Potential Causes, Journal of the Atmospheric Sciences, 60, 2496–2508, https://doi.org/10.1175/1520-0469(2003)060<2496:EGITNB>2.0.CO;2, https://doi.org/10.1175/1520-0469(2003)060%3C2496:EGITNB%3E2.0.COhttp://0.0.0.2, 2003.

Balsley, B. B., Frehlich, R. G., Jensen, M. L., and Meillier, Y.: High-Resolution In Situ Profiling through the Stable Boundary Layer: Examination of the SBL Top in Terms of Minimum Shear, Maximum Stratification, and Turbulence Decrease, Journal of the Atmospheric Sciences, 63, 1291–1307, https://doi.org/10.1175/JAS3671.1, https://doi.org/10.1175/JAS3671.1, 2006.

Balsley, B. B., Lawrence, D. A., Woodman, R. F., Fritts, D. C., Balsley, B. B., Lawrence, D. A., and Woodman, R. F.: Fine-Scale Characteristics of Temperature, Wind, and Turbulence in the Lower Atmosphere (0–1,300 m) Over the South Peruvian Coast, Boundary-Layer Meteorology, 147, 165–178, https://doi.org/10.1007/s10546-012-9774-x, https://link.springer.com/article/10.1007/s10546-012-9774-xhttps://doi.org/10.1007/s10546-012-9774-x, 2013.

Balsley, B. B., Lawrence, D. A., Fritts, D. C., Wang, L., Wan, K., and Werne, J.: Fine Structure, Instabilities, and Turbulence in the Lower Atmosphere: High-Resolution In Situ Slant-Path Measurements with the DataHawk UAV and Comparisons with Numerical Modeling, Journal of Atmospheric and Oceanic Technology, 35, 619–642, https://doi.org/10.1175/JTECH-D-16-0037.1, http://journals.ametsoc.org/doi/10.1175/JTECH-D-16-0037.1, 2018.

Barat, J.: SOME CHARACTERISTICS OF CLEAR-AIR TURBULENCE IN THE MIDDLE STRATOSPHERE., Journal of the Atmospheric Sciences, 39, 2553–2564, https://doi.org/10.1175/1520-0469(1982)039<2553:SCOCAT>2.0.CO;2, 1982.

Chimonas, G.: Steps, waves and turbulence in the stably stratified planetary boundary layer, Boundary-Layer Meteorology, 90, 397–421, https://doi.org/10.1023/A:1001709029773, 1999.

Coulman, C. E.: Vertical profiles of small-scale temperature structure in the atmosphere, Boundary-Layer Meteorology, 4, 169–177, https://doi.org/10.1007/BF02265230, 1973.

Coulman, C. E., Vernin, J., and Fuchs, A.: Optical seeing—mechanism of formation of thin turbulent laminae in the atmosphere, Applied Optics, 34, 5461–5474, https://doi.org/10.1364/AO.34.005461, http://ao.osa.org/abstract.cfm?URI=ao-34-24-5461, 1995.

Dalaudier, F., Sidi, C., Crochet, M., and Vernin, J.: Direct Evidence of "Sheets" in the Atmospheric Temperature Field, Journal of the Atmospheric Sciences, 51, 237–248, https://doi.org/10.1175/1520-0469(1994)051<0237:DEOITA>2.0.CO;2, https://doi.org/10.1175/1520-0469(1994)051%3C0237:DEOITA%3E2.0.COhttp://0.0.0.2, 1994.

de Boer, gijS de Boer, Ivey, M., SChMid, B., dale LaWrenCe, darielle DexheiMer, Mei, F., john HuBBe, alBerT Bendure, jaSper HardeSTy, Shupe, M., alliSon MCCoMiSkey, hagen Telg, SChMiTT, C., MaTroSov, S., ian BrookS, jeSSie CreaMean, aMy SoloMon, david Turner, WilliaMS, C., Maahn, M., ArgroW, B., Palo, S., Long, C., ru Shan Gao, jaMeS MaTher, de Boer, gijS de Boer, Ivey, M., SChMid, B., dale LaWrenCe, darielle DexheiMer, Mei, F., john HuBBe, alBerT Bendure, jaSper HardeSTy, Shupe, M., alliSon MCCoMiSkey, hagen Telg, SChMiTT, C., MaTroSov, S., ian BrookS, jeSSie CreaMean, aMy SoloMon, david Turner, WilliaMS, C., Maahn, M., ArgroW, B., Palo, S., Long, C., ru Shan Gao, and jaMeS MaTher: AFFILIATIONS: A BIRD'S-EYE VIEW Development of an Operational ARM Unmanned Aerial Capability for Atmospheric Research in Arctic Alaska, journals.ametsoc.org, 99, 1197–1212, https://doi.org/10.1175/BAMS-D-17-0156.1, https://journals.ametsoc.org/doi/abs/10.1175/BAMS-D-17-0156.1, 2018.

de Boer, G., Diehl, C., Jacob, J., Houston, A., Smith, S. W., Chilson, P., Schmale, D. G., Intrieri, J., Pinto, J., Elston, J., Brus, D., Kemppinen, O., Clark, A., Lawrence, D., Bailey, S. C. C., Sama, M. P., Frazier, A., Crick, C., Natalie, V., Pillar-Little, E., Klein, P., Waugh, S.,

Atmospheric
Measurement
Techniques
Discussions

Lundquist, J. K., Barbieri, L., Kral, S. T., Jensen, A. A., Dixon, C., Borenstein, S., Hesselius, D., Human, K., Hall, P., Argrow, B.,
Thornberry, T., Wright, R., and Kelly, J. T.: Development of community, capabilities and understanding through unmanned aircraft-based

365   atmospheric research: The LAPSE-RATE campaign, Bulletin of the American Meteorological Society, https://doi.org/10.1175/bams-d-
19-0050.1, 2019.

Eaton, F. D., Nastrom, G. D., Masson, B. S., Hahn, I. L., McCrae, K. A., Nowlin, S. R., and Berkopec, T. L.: Radar and aircraft observations
of a layer of strong refractivity turbulence, in: Proc.SPIE, vol. 3381, https://doi.org/10.1117/12.323944, 1998.

Fairall, C. W., White, A. B., and Thomson, D. W.: A stochastic model of gravity-wave-induced clear-air turbulence, Journal of the Atmo-

370   spheric Sciences, 48, 1771–1790, https://doi.org/10.1175/1520-0469(1991)048<1771:ASMOGW>2.0.CO;2, 1991.

Fernando, H. J. S., Pardyjak, E. R., Di Sabatino, S., Chow, F. K., De Wekker, S. F. J., Hoch, S. W., Hacker, J., Pace, J. C., Pratt, T., Pu,
Z., Steenburgh, W. J., Whiteman, C. D., Wang, Y., Zajic, D., Balsley, B., Dimitrova, R., Emmitt, G. D., Higgins, C. W., Hunt, J. C. R.,
Knievel, J. C., Lawrence, D., Liu, Y., Nadeau, D. F., Kit, E., Blomquist, B. W., Conry, P., Coppersmith, R. S., Creegan, E., Felton,
M., Grachev, A., Gunawardena, N., Hang, C., Hocut, C. M., Huynh, G., Jeglum, M. E., Jensen, D., Kulandaivelu, V., Lehner, M., Leo,

375   L. S., Liberzon, D., Massey, J. D., McEnerney, K., Pal, S., Price, T., Sghiatti, M., Silver, Z., Thompson, M., Zhang, H., and Zsedrovits,
T.: The materhorn : Unraveling the intricacies of mountain weather, Bulletin of the American Meteorological Society, 96, 1945–1968,
https://doi.org/10.1175/BAMS-D-13-00131.1, 2015.

Frehlich, R., Meillier, Y., Jensen, M. L., and Balsley, B.: Turbulence Measurements with the CIRES Tethered Lifting System dur-
ing CASES-99: Calibration and Spectral Analysis of Temperature and Velocity, Journal of the Atmospheric Sciences, 60, 2487–

380   2495, https://doi.org/10.1175/1520-0469(2003)060<2487:TMWTCT>2.0.CO;2, https://doi.org/10.1175/1520-0469(2003)060%3C2487:
TMWTCT%3E2.0.COhttp://0.0.0.2, 2003.

Fritts, D. C. and Rastogi, P. K.: Convective and dynamical instabilities due to gravity wave motions in the lower and middle atmo-
sphere: Theory and observations, Radio Science, 20, 1247–1277, https://doi.org/10.1029/RS020i006p01247, http://doi.wiley.com/10.
1029/RS020i006p01247, 1985.

385   Fritts, D. C. and Wang, L.: Gravity wave-fine structure interactions. Part II: Energy dissipation evolutions, statistics, and implications, Journal
of the Atmospheric Sciences, 70, 3735–3755, https://doi.org/10.1175/JAS-D-13-059.1, 2013.

Fritts, D. C., Wang, L., Werne, J., Lund, T., and Wan, K.: Gravity Wave Instability Dynamics at High Reynolds Numbers. Part
I: Wave Field Evolution at Large Amplitudes and High Frequencies, Journal of the Atmospheric Sciences, 66, 1126–1148,
https://doi.org/10.1175/2008JAS2726.1, https://journals.ametsoc.org/view/journals/atsc/66/5/2008jas2726.1.xml, 2009a.

390   Fritts, D. C., Wang, L., Werne, J., Lund, T., and Wan, K.: Gravity Wave Instability Dynamics at High Reynolds Numbers. Part II: Turbulence
Evolution, Structure, and Anisotropy, Journal of the Atmospheric Sciences, 66, 1149–1171, https://doi.org/10.1175/2008JAS2727.1, https:
//journals.ametsoc.org/view/journals/atsc/66/5/2008jas2727.1.xml, 2009b.

Fritts, D. C., Wang, L., and Werne, J. A.: Gravity Wave–Fine Structure Interactions. Part I: Influences of Fine Structure Form and Orientation
on Flow Evolution and Instability, Journal of the Atmospheric Sciences, 70, 3710–3734, https://doi.org/10.1175/JAS-D-13-055.1, http:

395   //journals.ametsoc.org/doi/abs/10.1175/JAS-D-13-055.1, 2013.

Fritts, D. C., Wang, L., Baumgarten, G., Miller, A. D., Geller, M. A., Jones, G., Limon, M., Chapman, D., Didier, J., Kjellstrand,
C. B., Araujo, D., Hillbrand, S., Korotkov, A., Tucker, G., and Vinokurov, J.: High-resolution observations and modeling of turbu-
lence sources, structures, and intensities in the upper mesosphere, Journal of Atmospheric and Solar-Terrestrial Physics, 162, 57–78,
https://doi.org/10.1016/j.jastp.2016.11.006, http://dx.doi.org/10.1016/j.jastp.2016.11.006, 2017.

400   Fritts, D. C., Miller, A. D., Kjellstrand, C. B., Geach, C., Williams, B. P., Kaifler, B., Kaifler, N., Jones, G., Rapp, M., Limon, M., Reimuller, J., Wang, L., Hanany, S., Gisinger, S., Zhao, Y., Stober, G., and Randall, C. E.: PMC Turbo: Studying Gravity Wave and Instability Dynamics in the Summer Mesosphere Using Polar Mesospheric Cloud Imaging and Profiling From a Stratospheric Balloon, Journal of Geophysical Research: Atmospheres, 124, 6423–6443, https://doi.org/10.1029/2019JD030298, 2019.

Fritts, D. C., Wang, L., Lund, T. S., and Thorpe, S. A.: Multi-Scale Dynamics of Kelvin-Helmholtz Instabilities . Part 1 : Secondary Instabil-
405   ities and the Dynamics of Tubes and Knots, Journal of Fluid Mechanics, submitted, pp. 1–27, 2021a.

Fritts, D. C., Wang, L., Thorpe, S. A., and Lund, T. S.: Multi-Scale Dynamics of Kelvin-Helmholtz Instabilities . Part 2 : Energy Dissipation Rates , Evolutions , and Statistics, Journal of Fluid Mechanics, submitted, pp. 1–39, 2021b.

Fua, D., Chimonas, G., Einaudi, F., and Zeman, O.: ANALYSIS OF WAVE-TURBULENCE INTERACTION., Journal of the Atmospheric Sciences, 39, 2450–2463, https://doi.org/10.1175/1520-0469(1982)039<2450:AAOWTI>2.0.CO;2, 1982.

410   Gage, K. S. and Balsley, B. B.: On the scattering and reflection mechanisms contributing to clear air radar echoes from the tropo-
sphere, stratosphere, and mesophere, Radio Science, 15, 243–257, https://doi.org/10.1029/RS015i002p00243, https://doi.org/10.1029/RS015i002p00243, 1980.

Gage, K. S. and Green, J. L.: Evidence for specular reflection from monostatic VHF radar observations of the stratosphere, Radio Science, 13, 991–1001, https://doi.org/10.1029/RS013i006p00991, https://doi.org/10.1029/RS013i006p00991, 1978.

415   Geach, C., Hanany, S., Fritts, D. C., Kaifler, B., Kaifler, N., Kjellstrand, C. B., Williams, B. P., Eckermann, S. D., Miller, A. D., Jones, G., and Reimuller, J.: Gravity Wave Breaking and Vortex Ring Formation Observed by PMC Turbo, Journal of Geophysical Research: Atmospheres, 125, 0–3, https://doi.org/10.1029/2020JD033038, 2020.

Gossard, E. E., Chadwick, R. B., Detman, T. R., and Gaynor, J.: Capability of Surface-Based Clear-Air Doppler Radar for Monitoring Meteorological Structure of Elevated Layers, Journal of Climate and Applied Meteorology, 23, 474–485, https://doi.org/10.1175/1520-
420   0450(1984)023<0474:COSBCA>2.0.CO;2,   https://doi.org/10.1175/1520-0450(1984)023%3C0474:COSBCA%3E2.0.COhttp://0.0.0.2, 1984.

Hecht, J. H., Fritts, D. C., Gelinas, L. J., Rudy, R. J., Walterscheid, R. L., and Liu, A. Z.: Kelvin-Helmholtz Billow Interactions and In-
stabilities in the Mesosphere Over the Andes Lidar Observatory: 1. Observations, Journal of Geophysical Research: Atmospheres, 126, https://doi.org/10.1029/2020JD033414, 2021.

425   Hunt, J. C. R., Kaimal, J. C., and Gaynor, J. E.: Some observations of turbulence structure in stable layers, Quarterly Journal of the Royal Meteorological Society, 111, 793–815, https://doi.org/10.1002/qj.49711146908, https://doi.org/10.1002/qj.49711146908, 1985.

Kantha, L., Lawrence, D., Luce, H., Hashiguchi, H., Tsuda, T., Wilson, R., Mixa, T., and Yabuki, M.: Shigaraki UAV-Radar Ex-
periment (ShUREX): overview of the campaign with some preliminary results, Progress in Earth and Planetary Science, 4, https://doi.org/10.1186/s40645-017-0133-x, 2017.

430   Kantha, L., Luce, H., Hashiguchi, H., and Doddi, A.: Atmospheric structures in the troposphere as revealed by high-resolution backscatter images from MU radar operating in range-imaging mode, Progress in Earth and Planetary Science, 6, 32, https://doi.org/10.1186/s40645-019-0274-1, https://doi.org/10.1186/s40645-019-0274-1, 2019.

Knievel, J. C., Liu, Y., Hopson, T. M., Shaw, J. S., Halvorson, S. F., Fisher, H. H., Roux, G., Sheu, R.-s., Pan, L., Hacker, J. P., Vernon, E., Gallagher Iii, F. W., and Pace, J. C.: Mesoscale Ensemble Weather Prediction at U.S. Army Dugway Proving Ground, Utah, jour-
435   nals.ametsoc.org, 32, 2195–2216, https://doi.org/10.1175/WAF-D-17-0049.1, www.ametsoc.org/PUBSReuseLicenses, 2017.

Lawrence, D. A. and Balsley, B. B.: Design of a low-cost UAS for high-resolution atmospheric sensing, in: AIAA Infotech at Aerospace (I at A) Conference, https://doi.org/10.2514/6.2013-4669, 2013.

Lawrence, D. A., Frew, E. W., and Pisano, W. J.: Lyapunov Vector Fields for Autonomous Unmanned Aircraft Flight Control, arc.aiaa.org, 31, 1220–1229, https://doi.org/10.2514/1.34896, http://arc.aiaa.org, 2008.

440 Liu, Y., Warner, T. T., Bowers, J. F., Carson, L. P., Chen, F., Clough, C. A., Davis, C. A., Egeland, C. H., Halvorson, S. F., Huck, T. W., Lachapelle, L., Malone, R. E., Rife, D. L., Sheu, R.-S., Swerdlin, S. P., and Weingarten @@, D. S.: The Operational Mesogamma-Scale Analysis and Forecast System of the U.S. Army Test and Evaluation Command. Part I: Overview of the Modeling System, the Forecast Products, and How the Products Are Used, journals.ametsoc.org, 47, 1077–1092, https://doi.org/10.1175/2007JAMC1653.1, https://journals.ametsoc.org/doi/abs/10.1175/2007JAMC1653.1, 2008.

445 Luce, H., Crochet, M., Dalaudier, F., and Sidi, C.: Interpretation of VHF ST radar vertical echoes from in situ temperature sheet observations, Radio Science, 30, 1003–1025, https://doi.org/10.1029/95RS00713, https://doi.org/10.1029/95RS00713, 1995.

Luce, H., Fukao, S., Yamamoto, M., Sidi, C., and Dalaudier, F.: Validation of Winds Measured by MU Radar with GPS Radioson-des during the MUTSI Campaign, Journal of Atmospheric and Oceanic Technology, 18, 817–829, https://doi.org/10.1175/1520-0426(2001)018<0817:VOWMBM>2.0.CO;2, https://doi.org/10.1175/1520-0426(2001)018%3C0817:VOWMBM%3E2.0.COhttp://0.0.

450 0.2, 2001.

Luce, H., Kantha, L., Hashiguchi, H., Lawrence, D., Yabuki, M., Tsuda, T., and Mixa, T.: Comparisons between high-resolution profiles of squared refractive index gradient M 2 measured by the Middle and Upper Atmosphere Radar and unmanned aerial vehicles (UAVs) during the Shigaraki UAV-Radar Experiment 2015 campaign, 35, 423–441, https://doi.org/10.5194/angeo-35-423-2017, www.ann-geophys.net/35/423/2017/, 2017.

455 Luce, H., Kantha, L., Hashiguchi, H., Lawrence, D., and Doddi, A.: Turbulence kinetic energy dissipation rates estimated from concurrent UAV and MU radar measurements, Earth, Planets and Space, 70, https://doi.org/10.1186/s40623-018-0979-1, 2018a.

Luce, H., Kantha, L., Hashiguchi, H., Lawrence, D., Mixa, T., Yabuki, M., and Tsuda, T.: Vertical structure of the lower troposphere derived from MU radar, unmanned aerial vehicle, and balloon measurements during ShUREX 2015, Progress in Earth and Planetary Science, 5, https://doi.org/10.1186/s40645-018-0187-4, 2018b.

460 Luce, H., Kantha, L., Hashiguchi, H., and Lawrence, D.: Estimation of Turbulence Parameters in the Lower Troposphere from ShUREX (2016–2017) UAV Data, https://doi.org/10.3390/atmos10070384, 2019.

Mahrt, L.: Stratified Atmospheric Boundary Layers, Boundary-Layer Meteorology, 90, 375–396, https://doi.org/10.1023/A:1001765727956, https://doi.org/10.1023/A:1001765727956, 1999.

Miller, A. D., Fritts, D. C., Chapman, D., Jones, G., Limon, M., Araujo, D., Didier, J., Hillbrand, S., Kjellstrand, C. B., Korotkov, A., Tucker,

465 G., Vinokurov, Y., Wan, K., and Wang, L.: Stratospheric imaging of polar mesospheric clouds: A new window on small-scale atmospheric dynamics, Geophysical Research Letters, 42, 6058–6065, https://doi.org/10.1002/2015GL064758, 2015.

Muschinski, A. and Wode, C.: First In Situ Evidence for Coexisting Submeter Temperature and Humidity Sheets in the Lower Free Tro-posphere, Journal of the Atmospheric Sciences, 55, 2893–2906, https://doi.org/10.1175/1520-0469(1998)055<2893:FISEFC>2.0.CO;2, https://doi.org/10.1175/1520-0469(1998)055%3C2893:FISEFC%3E2.0.COhttp://0.0.0.2, 1998.

470 Muschinski, A., Frehich, R., Jensen, M., Hugo, R., Hoff, A., Eaton, F., Balsley, B., Frehlich, R., Jensen, M., Hugo, R., Hoff, A., Eaton, F., and Balsley, B.: Fine-Scale Measurements Of Turbulence In The Lower Troposphere: An Intercomparison Be-tween A Kite- And Balloon-Borne, And A Helicopter-Borne Measurement System, Boundary-Layer Meteorology, 98, 219–250, https://doi.org/10.1023/A:1026520618624, https://doi.org/10.1023/A:1026520618624, 2001a.

Muschinski, A., Frehlich, R., Jensen, M., Hugo, R., Hoff, A., Eaton, F., and Balsley, B.: Fine-scale measurements of turbulence in the
lower troposphere: An intercomparison between a kit-and balloon-borne, and a helicopter-borne measurement system, Boundary-Layer
Meteorology, 98, 219–250, https://doi.org/10.1023/A:1026520618624, 2001b.

Parsons, D., Dabberdt, W., Cole, H., Hock, T., Martin, C., Barrett, A.-L., Miller, E., Spowart, M., Howard, M., Ecklund, W., Carters, D.,
Gage, K., and Wilson, J.: The Integrated Sounding System: Description and Preliminary Observations from TOGA COARE, Bulletin of
the American Meteorological Society, 75, 553–568, https://doi.org/10.1175/1520-0477(1994)075<0553:TISSDA>2.0.CO;2, https://doi.
org/10.1175/1520-0477(1994)075%3C0553:TISSDA%3E2.0.COhttp://0.0.0.2, 1994.

Röttger, J.: Structure and dynamics of the stratosphere and mesosphere revealed by VHF radar investigations, pure and applied geophysics,
118, 494–527, https://doi.org/10.1007/BF01586465, https://doi.org/10.1007/BF01586465, 1980.

Röttger, J. and Liu, C. H.: Partial reflection and scattering of VHF radar signals from the clear atmosphere, Geophysical Research Letters, 5,
357–360, https://doi.org/10.1029/GL005i005p00357, https://doi.org/10.1029/GL005i005p00357, 1978.

Scipión, D. E., Lawrence, D. A., Milla, M. A., Woodman, R. F., Lume, D. A., and Balsley, B. B.: Simultaneous observations of structure func-
tion parameter of refractive index using a high-resolution radar and the DataHawk small airborne measurement system, ann-geophys.net,
34, 767–780, https://doi.org/10.5194/angeo-34-767-2016, www.ann-geophys.net/34/767/2016/, 2016.

Sidi, C., Lefrere, J., Dalaudier, F., and Barat, J.: An improved atmospheric buoyancy wave spectrum model, Journal of Geophysical Research:
Atmospheres, 93, 774–790, https://doi.org/10.1029/JD093iD01p00774, https://doi.org/10.1029/JD093iD01p00774, 1988.

Smith, S. A., Fritts, D. C., and Vanzandt, T. E.: Evidence for a Saturated Spectrum of Atmospheric Gravity Waves, Journal of the
Atmospheric Sciences, 44, 1404–1410, https://doi.org/10.1175/1520-0469(1987)044<1404:EFASSO>2.0.CO;2, https://doi.org/10.1175/
1520-0469(1987)044%3C1404:EFASSO%3E2.0.COhttp://0.0.0.2, 1987.

Tjernström, M., Balsley, B. B., Svensson, G., and Nappo, C. J.: The Effects of Critical Layers on Residual Layer Turbulence, Journal of the
Atmospheric Sciences, 66, 468–480, https://doi.org/10.1175/2008JAS2729.1, https://doi.org/10.1175/2008JAS2729.1, 2009.

VanZandt, T. E., Green, J. L., Gage, K. S., and Clark, W. L.: Vertical profiles of refractivity turbulence structure constant: Comparison of
observations by the Sunset Radar with a new theoretical model, Radio Science, 13, 819–829, https://doi.org/10.1029/RS013i005p00819,
1978.

Woodman, R. F. and Chu, Y.: Aspect sensitivity measurements of VHF backscatter made with the Chung-Li radar: Plausible mechanisms,
Radio Science, 24, 113–125, https://doi.org/10.1029/RS024i002p00113, 1989.

Woodman, R. F. and Guillen, A.: Radar Observations of Winds and Turbulence in the Stratosphere and Mesosphere, Journal of the
Atmospheric Sciences, 31, 493–505, https://doi.org/10.1175/1520-0469(1974)031<0493:ROOWAT>2.0.CO;2, https://doi.org/10.1175/
1520-0469(1974)031%3C0493:ROOWAT%3E2.0.COhttp://0.0.0.2, 1974.

Xing-Sheng, L., Gaynor, J. E., and Kaimal, J. C.: A study of multiple stable layers in the nocturnal lower atmosphere, Boundary-Layer
Meteorology, 26, 157–168, https://doi.org/10.1007/BF00121540, https://doi.org/10.1007/BF00121540, 1983.